

Analysis of Beauty Production and Hadronization in Vacuum and Quark-Gluon Plasma with CMS

by

Zhaozhong Shi

B.A., University of California, Berkeley (2016)

Submitted to the Department of Physics
in partial fulfillment of the requirements for the degree of
Doctor of Philosophy in Physics

at the

MASSACHUSETTS INSTITUTE OF TECHNOLOGY

September 2021

© Massachusetts Institute of Technology 2021. All rights reserved.

Author
Department of Physics
September 5, 2021

Certified by
Yen-Jie Lee
Associate Professor
Thesis Supervisor

Accepted by
Nergis Mavalvala
Associate Department Head of Physics

Analysis of Beauty Production and Hadronization in Vacuum and Quark-Gluon Plasma with CMS

by

Zhaozhong Shi

Submitted to the Department of Physics
on September 5, 2021, in partial fulfillment of the
requirements for the degree of
Doctor of Philosophy in Physics

Abstract

A novel analysis of fully reconstructed B_s^0 , B^0 , and B^+ mesons decay into J/ψ and strange hadrons using Compact Muon Solenoid (CMS) Experiment 2017 pp dataset and 2018 PbPb data at the center of mass energy per nucleon $\sqrt{s_{NN}} = 5.02$ TeV at the Large Hadron Collider (LHC) is presented in this thesis. We apply machine learning techniques to obtain significant B-meson signals and extend the kinematic regime of B-meson measurements. In our analysis, B_s^0 signal of greater than 5σ significance is first confirmed in heavy-ion collisions. The inclusive beauty production cross section in pp collisions from the B^+ exclusive decay cross section down to zero transverse momentum is measured. The precise measurement of B-meson nuclear modification factor and B_s^0/B^+ ratio and the comparisons with theoretical model predictions will also be discussed. Our results will help elucidate the beauty production and hadronizaton mechanisms in vacuum and quark-gluon plasma at the LHC energy.

Thesis Supervisor: Yen-Jie Lee
Title: Associate Professor

Acknowledgments

This is the acknowledgements section. You should replace this with your own acknowledgements.

Contents

1	Introduction	21
1.1	The Standard Model of Particle Physics	21
1.2	Quantum Chromodynamics	22
1.2.1	QCD Lagrangian	22
1.2.2	Asymptotic Freedom	23
1.2.3	Perturbative QCD	24
1.2.4	Non-perturbative QCD	25
1.2.5	QCD Factorization Theorem	25
1.2.6	Color Confinement	26
1.2.7	Hadronization	26
1.3	QCD In Extreme Conditions	27
1.3.1	QCD at Finite Temperature	27
1.3.2	Melting of QCD Vacuum	28
1.3.3	Chiral Symmetry Restoration	28
1.3.4	Temperature Dependence of QCD Static Potential	30
1.3.5	Hadron Mass Spectrum and Hagedorn Temperature	31
1.3.6	Color Deconfinement	32
1.3.7	QCD at High Parton Density	32
1.3.8	Color Glass Condensate	33
1.3.9	Gluon Saturation	33
1.3.10	Nuclear Shadowing	34
1.4	QCD Matter	34

1.4.1	QCD Phase Diagram	34
1.4.2	Hadron Resonance Gas	36
1.4.3	Quark-Gluon Plasma	37
1.4.4	Color Superconductor	38
1.4.5	Phase Transition	39
1.4.6	Critical Point	40
1.5	High Energy Nuclear Physics	40
1.5.1	Laboratories	40
1.5.2	Relativistic Heavy Ion Collider (RHIC)	41
1.5.3	Large Hadron Collider (LHC)	43
1.5.4	High Energy Physics Coordinates	45
1.5.5	Stages of Heavy-Ion Collisions	47
1.5.6	Global Event Observables	48
1.5.7	Glauber Model	51
1.6	Characterization of Quark-Gluon Plasma	55
1.6.1	Signatures	56
1.6.2	Discovery	66
1.6.3	Macroscopic Properties	67
1.6.4	Microscopic Structure	67
1.6.5	Open Questions	70
1.7	Hard Probes	70
1.7.1	Jets	70
1.7.2	Electroweak Probes	70
1.7.3	Heavy Quarks	70
1.8	Open Heavy Flavor Physics	70
1.8.1	Heavy Quark Diffusion	70
1.8.2	Heavy Quark Energy Loss	70
1.8.3	Heavy Quark Hadronization	70
1.8.4	Experimental Observables	70

2 The CMS Detector	71
2.1 Overview	72
2.2 Triggers	72
2.2.1 L1 Hardware Trigger	72
2.2.2 HLT Trigger	72
2.3 Tracking System	72
2.3.1 Silicon Pixel Detector	72
2.3.2 Silicon Strip Detector	72
2.3.3 Tracking Algorithm	72
2.4 Muon System	72
2.5 Calorimeter System	72
2.5.1 ECAL	72
2.5.2 HCAL	72
2.5.3 Forward HCAL	72
3 Experimental Procedures	73
3.1 Experimental Setup	73
3.2 LHC Heavy-Ion Run	73
3.3 Minimum Biased Trigger	73
3.4 Dimuon Trigger	73
3.5 Run Monitoring	73
3.6 Data Acquisition	73
4 Technical Objects	75
4.1 Hits	75
4.2 Clusters	75
4.3 Tracks	75
4.4 Vertices	75
4.5 Muons	75

5 Data Analysis	77
5.1 Analysis Strategies	78
5.1.1 Physics Goals	78
5.1.2 General Workflow	78
5.1.3 Technical Challenges	78
5.2 Global Event Observables	78
5.2.1 Total Number of Events	78
5.2.2 Centrality Definition	78
5.2.3 Number of Participants Nucleons	78
5.2.4 Number of Binary Collisions	78
5.2.5 Event Multiplicity	78
5.3 Monte Carlo Simulations	78
5.3.1 PYTHIA	78
5.3.2 Hydjet Embedding	78
5.3.3 EvtGen Package	78
5.3.4 Reweighting	78
5.4 B meson Reconstruction	78
5.4.1 Decay Channels	78
5.4.2 Event Selections	78
5.4.3 Track and Muon Selections	78
5.4.4 Results	78
5.5 Cut Optimization	78
5.5.1 Topological Variables	78
5.5.2 Multivariate Analysis	78
5.5.3 Machine Learning Techniques	78
5.5.4 Training Performance	78
5.5.5 Working Point Determination	78
5.6 Signal Extraction	78
5.6.1 B-meson Invariant Mass Distributions	78
5.6.2 Fitting Models	78

5.6.3	Raw Yield Extraction	78
5.6.4	Signal Significance Estimation	78
5.7	Acceptance and Efficiency Correction	78
5.7.1	Analysis Challenges	78
5.7.2	Fiducial Measurement	78
5.7.3	Fine 2D Efficiency Map	78
5.7.4	Data-Drive Efficiency Correction	78
5.7.5	Tag & Probe Techniques	78
5.7.6	Nominal Results	78
5.8	Cross Section Results	78
5.9	Validation Tests	78
5.9.1	Mass Scraping Test	78
5.9.2	Raw Yield Closure	78
5.9.3	Efficiency Closure	78
5.9.4	sPlot Closure	78
5.10	Statistical Uncertainties Determination	78
5.10.1	Data Bootstrapping	78
5.10.2	Statistical Uncertainties Interpretation	78
5.11	Systematic Uncertainties Estimation	78
5.11.1	Global Observables	78
5.11.2	Branching Ratios	78
5.11.3	Tracking Efficiency	78
5.11.4	Muon Efficiency	78
5.11.5	Selection Efficiency	78
5.11.6	Signal Extraction	78
5.11.7	Summary	78
5.12	Final Results	78
5.12.1	B_s^0 and B^+ Cross Section	78
5.12.2	B_s^0/B^+ Ratio	78
5.12.3	B_s^0 and B^+ Nuclear Modification Factor	78

6 Conclusions	79
6.1 Comparison with Other Experiments and Theoretical Models	79
6.2 Physics Messages Discussion	79
6.3 Conclusions	79
6.4 Future Outlooks	79
7 Other Studies	81
7.1 sPHENIX Heavy Flavor Physics Simulations	81
7.2 sPHENIX Electromagnetic Calorimeter Studies	81
7.3 EIC Electromagnetic Calorimeter R&D	81
A Tables	83
B Figures	85
List of Symbols	89
Abbreviations	91

List of Figures

1-1	The 17 elementary particles, including leptons, quarks, gauge bosons, and Higgs boson, and their basic properties, such as mass, electric charge, spin, in the Standard Model of Particles Physics are shown above.	22
1-2	The running of the strong coupling constant α_s in different experiments at different energy scale Q and the comparison with QCD calculations are shown above.	24
1-3	The QCD factorization theorem applied to a pp collision event involving in soft and hard processes are shown above.	25
1-4	The fragmentation process of charms quarks hadronize into D^\pm (left) and the coalescence process of beauty quark with a strange quark nearby to form a B_s^0 are shown above.	27
1-5	Many-body dynamics of QCD in different physics limits is shown above.	27
1-6	The Feynman diagram of a triangular quark loop under external magnetic field B describe the generation of chiral magnetic current via chiral anomaly is shown above.	29
1-7	The schematics of charge separation due chirality imbalance of quarks under a strong magnetic field in heavy-ion collisions, know as Chiral Magnetic Effect, is shown above.	30
1-8	The QCD potential $V(r)$ from at zero and at finite temperatures as a function of distance r is shown above. Here, the critical temperature $T_c = 192$ MeV. We can see that the QCD saturates at a finite value at finite temperature.	31

1-9	The double-log scale of energy landscape $\ln x$ and the virtuality $\ln Q^2$ diagram picturing the different regimes of the hadron wave function, the saturation line separates the dilute (DGLAP) regime from the dense (saturation) regime is shown above.	34
1-10	The P-T diagram of water in gas, liquid, solid phases is shown above.	35
1-11	The theoretical QCD phase diagram of different QCD matter, including hadron resonance gas, quark-gluon plasma, neutron star, and color superconductor, as function of temperature and baryon chemical potential is shown above. The solid line indicates the conjecture of first order phase transition between quark-gluon plasma and hadron gas while the dash line is a smooth crossover.	35
1-12	The schematic plot of potential energy between two nucleon via pion exchange as a function of distance is shown above [53]. This potential with a well minimizing near 100 MeV allow nucleons to bind together and form atomic nuclei and nuclear matter.	36
1-13	The pressure and energy density from lattice simulation compared with ideal hadron resonance gas and Van der Waas interaction at different $\frac{\mu_B}{T}$ are shown above.	37
1-14	Predictions the normalized pressure to the stefan Boltzmann pressure $P_{SB} = \sigma T^4$ as a function of temperature T for three-flavor QGP obtained from lattice QCD, the MIT bag model and perturbative QCD including their uncertainties bands are shown.	39
1-15	The overview of RHIC at BNL from the sky view is shown above. The actual locations of other accelerator facilities at BNL, including Linac, Booster, EBIS, NSRL, AGS, and the experiments at RHIC,STAR and PHENIX, are also labelled.	42
1-16	The acceleration of gold ions for RHIC is shown above.	43
1-17	The overview of LHC at CERN from the sky view is shown above. The actual locations of the experiments at the LHC, ATLAS, CMS, ALICE and LHCb, as well as the French-Swiss border, are also labelled.	44

1-18 The schematic overview of CERN accelerator complex with the accelerators labelled is shown above. Proton and lead ion are accelerated using these facilities to boost to the energy scale of TeV.	45
1-19 The cylindrical coordinate system in the position space (left) and the space time diagram (right) for relativistic heavy-ion physics analysis are shown above.	46
1-20 An event of a typical heavy-ion collisions event with different stages as time evolves is shown above.	48
1-21 The space-time evolution of heavy-ion collisions is shown above. It consists of four stages: initial state before the collision, the creation of quark-gluon plasma right after of the collision, hadronization after quark-gluon plasma expands and cools down, and the freeze-out stage when the inelastic scattering process ceases.	49
1-22 The definition of impact parameter b in heavy-ion collision and the overlapping interaction region and the break up remnants of the two nuclei, which is called spectator, moving in the z-direction are shown above. We can also see that heavy-ion collisions have an almond shape interaction region, which results in the azimuthal anisotropic emission of final state particles.	50
1-23 The plot showing relationship among number of charged particle, N_{ch} , related to the number of participating nucleon N_{part} , the differential cross section $\frac{d\sigma}{dN_{ch}}$, and the centrality, according to the Glauber Model calculations, is shown above.	52
1-24 Two gold ions collide head-on in the STAR detector. The event with reconstructed tracks of final state particles are display by STAR TPC shown above.	52

1-34 The yield ratio of ϕ/π as a function N_{part} in p + p, p + Au, and Au + Au from the STAR experiment at RHIC (left) and strange hadrons $K_s^0, \Lambda^+, \Xi^0, \Omega^-$ as a function of $dN_c h/d\eta$ from the ALICE experiment at LHC are shown above. We can see a clear trend of the increase of the strange hadron to pion ratio as the event multiplicity increases. In addition, we also see that the ϕ/π ratio increases as $\sqrt{s_{NN}}$ increases, which suggests the strangeness content enhances as the temperature of the system increase.	67
1-35 The announcement of discover of QGP in a special seminar at CERN on February 10 2000 is shown above.	68
1-36 The nuclear modifications factor R_{AA} of fully reconstructed Υ as a function of N_{part} measured by the STAR experiment (left) at RHIC and CMS experiment (right) at the LHC are shown above. We can see that R_{AA} of the three Υ states is below 1 for both $N_{part} > 3$. The $J/\psi R_{AA}$ decreases as N_{part} increases, consistent to the increasing creation probability of QGP with larger N_{part} . In addition, a sequential suppression of ΥR_{AA} is observed by the CMS experiment: $R_{AA}^{\Upsilon(1S)} > R_{AA}^{\Upsilon(2S)} > R_{AA}^{\Upsilon(3S)}$, which agrees with the expectation QGP color screening effect.	69
B-1 Armadillo slaying lawyer.	85
B-2 Armadillo eradicating national debt.	86

List of Tables

A.1 Armadillos	83
--------------------------	----

Chapter 1

Introduction

1.1 The Standard Model of Particle Physics

Physics is the research of relationship between space and time and energy and matter. Physicists enjoy searching for symmetries and consideration laws in nature. They develop elegant mathematical formulations to describe the beauty of the nature and predict or explain the experimental results and observed phenomena.

There are four known fundamental forces in nature: gravitational force, electromagnetic force, strong force, and weak force. The gravitation force describes the interaction between two massive objects. The electromagnetic force describes the interaction between electrically charged objects. The strong force describes the interaction between nucleons. The weak force describes the radioactive decay of particles. The Standard Model (SM) of Particle Physics is based on theoretical of relativistic quantum field theory with a gauge symmetry of $SU(3) \times SU(2) \times U(1)$ [1]. It unifies the strong, weak, and electromagnetic into a single theory and describes all particles participating in these interactions. The ingredient of the standard model are lepton, quarks, gauge boson, and Higgs boson shown in Figure 1-1.

There are 19 parameters in the Standard Model: 6 quark masses, 3 lepton masses, 3 coupling strengths, 4 CKM angles, Higgs mass, vacuum expectation value, and QCD vacuum angle. These parameters are determined from the experiments. Physicists perform calculations based on the Standard Model and predict the cross section

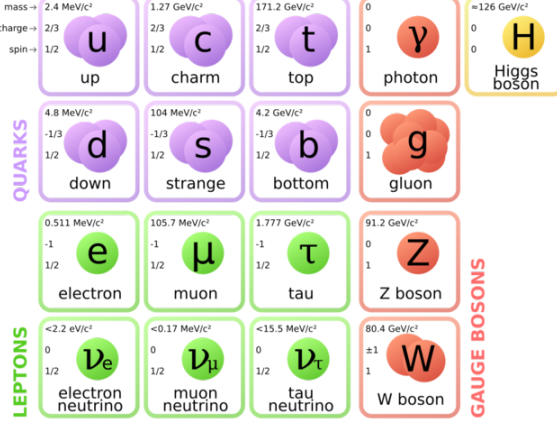


Figure 1-1: The 17 elementary particles, including leptons, quarks, gauge bosons, and Higgs boson, and their basic properties, such as mass, electric charge, spin, in the Standard Model of Particles Physics are shown above.

of different processes in high energy physics experiments. Since it is proposed in the 1970s, the Standard Model has been tested extensively in countless high-energy physics experiments. Its prediction holds for all of them with very few exceptions. The Standard Model consists of two sectors: the Electroweak theory (EW) and Quantum Chromodynamics (QCD). The Lagrangian of the Standard Model can be written as the sum of EW and QCD: $\mathcal{L}_{SM} = \mathcal{L}_{EW} + \mathcal{L}_{QCD}$

1.2 Quantum Chromodynamics

1.2.1 QCD Lagrangian

QCD, a non-abelian gauge theory with $SU(3)$ symmetry, is the theory for the strong interaction between quarks and gluons. The QCD Lagrangian is as follows:

$$\mathcal{L}_{QCD} = \bar{\Psi}^i i(\not{D})_{ij} \Psi^j - m \bar{\Psi}^i \Psi_i - \frac{1}{16\pi^2} G_a^{\mu\nu} G_a^{\mu\nu} \quad (1.1)$$

Where

$$\not{D} = \gamma^\mu \partial_\mu - ig_s \frac{\lambda}{2} \gamma^\mu A_\mu \quad (1.2)$$

$$G_a^{\mu\nu} = \partial^\mu A_a^\nu - \partial_\nu A_a^\mu + g_s f_{abc} A_b^\mu A_c^\nu \quad (1.3)$$

Here, λ are the Gell-Mann Matrices. f_{abc} is the structure of constant of $SU(3)$. A^μ is the eight gluon field. g_s is the strong coupling constant. The color indices i and j run from 1 to 3, which stands for 3 colors: red, blue, and green. The gluon field indices a , b , and c run from 1 to 8, standing for the 8 gluon state (Gluon octet as the combination of 3 color and 3 anticolor: $3 \times \bar{3} = 1 \oplus 8$) living in the adjoint representation of $SU(3)$ of color.

1.2.2 Asymptotic Freedom

The running of the strong coupling constant $\alpha_s = \frac{g_s^2}{4\pi}$ according to the 1-loop calculations in the renormalization theory [2] is shown as follows

$$\alpha_s(Q^2) = \frac{12\pi}{(11N_c - 2N_f) \ln(\frac{Q^2}{\Lambda_{QCD}^2})} \quad (1.4)$$

We can see that as the energy scale increases, the coupling strength of the strong interaction decreases. This is in contrast to QED where the electromagnetic coupling strength increases as the energy scale increases. In the ultra-violate limit $Q^2 \rightarrow \infty$ and $\alpha_s \rightarrow 0$, quarks and gluons behave like free particles. This feature in QCD is call Asymptotic Freedom [4]. Meanwhile, in the infrared limit, the strong coupling constant increases. Near the $\Lambda_{QCD} \simeq 100$ MeV, the coupling is greater than 1, where the perturbative expansion of QCD breaks down. Experimentally, physicists measure the strong coupling constant at different energy scales from different experiments at different colliders. Figure 1-2 [3] show the running of strong coupling constant in experiment and comparison with the theoretical calculations

An excellent agreement between the theoretical predictions and experimental results of the strong coupling constant is observed in Figure 1-2.

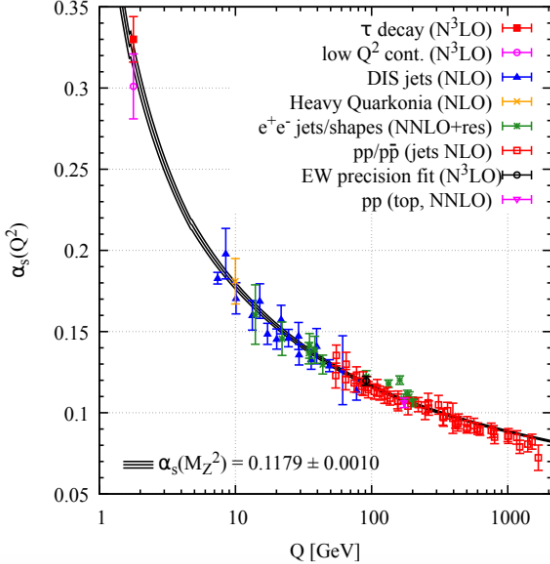


Figure 1-2: The running of the strong coupling constant α_s in different experiments at different energy scale Q and the comparison with QCD calculations are shown above.

1.2.3 Perturbative QCD

It is mathematically proven that there is in general no closed form expression for the Standard Model Lagrangian under the Quantum Field Theory framework. Therefore, physicist develop perturbation theory in Quantum Field Theory and apply it to the Standard Model. Physicist obtain asymptotic expansions as power series of the coupling constants and approximately calculate the expectation values of the observables to prediction experimental results.

For QCD, in high energy and hard scattering processes, since the coupling constant is much less than 1, perturbation theory is applicable to QCD. Feynman rules and diagrams are applicable in the matrix element to evaluate the cross section of hard parton-parton scattering. Perturbative QCD (pQCD) calculations have been tested various experiments such as electron positron annihilation, deep inelastic electron proton scattering, and high energy proton-proton collisions.

1.2.4 Non-perturbative QCD

At low energy and soft scattering processes, the coupling constant is greater than 1, perturbation theory of QCD breaks down. Many low-energy QCD processes such as hadronization and hadron-hadron interactions are non-perturbative. Historically, physicists developed Lattice gauge theory such as Lattice QCD to calculate the mass [5] of the proton and effective theory such as Chiral Perturbation Theory to study pion-nucleon scattering [6]. Non-perturbative QCD have achieved many successes. Currently, many novel developments applying non-perturbative QCD to understand nuclear structure and nucleon spin structure are being carried by physicists.

1.2.5 QCD Factorization Theorem

The QCD factorization theorem states that in events involving both hard and soft QCD processes, hard and soft process are mathematically factorized in the cross section computation as follows [7]:

$$\sigma_X = \sum \int dx_1 dx_2 f_i(x_1, \mu_F^2) f_j(x_2, \mu_F^2) \times \hat{\sigma}_{ij \rightarrow X}(p_1, p_2, \mu_R^2, \mu_F^2) \quad (1.5)$$

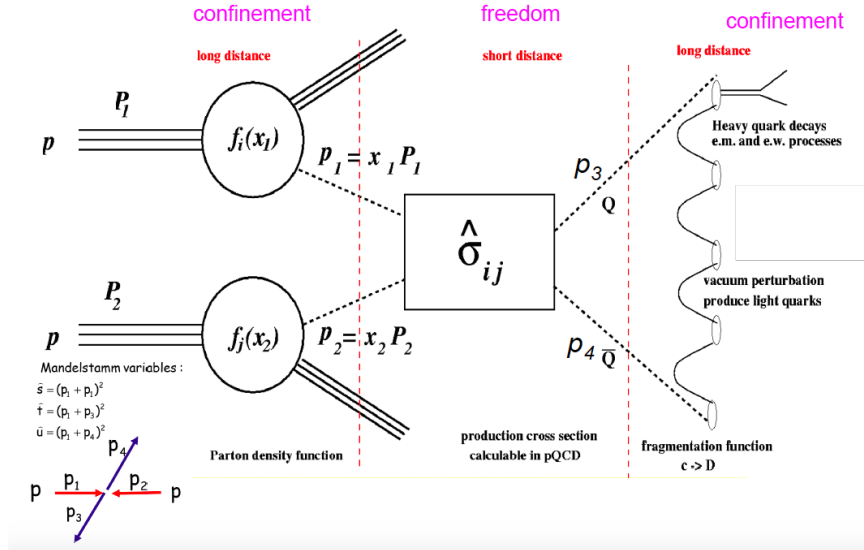


Figure 1-3: The QCD factorization theorem applied to a $p\bar{p}$ collision event involving in soft and hard processes are shown above.

The hard processes are encoded in the factor of partonic cross sections while the soft processes are measured in experiments. Physicists developed parton distribution function to describe initial kinematic of partons inside hadrons and fragmentation function to describe the parton hadronization process. Both parton distribution function and fragmentation function are measured in experiments.

Physicists apply QCD factorization theorem to perform pQCD calculation of hard scattering processes and use the measurement from the to understand the hadron spectroscopy in electron-positron, electron-proton, and proton-proton collisions.

1.2.6 Color Confinement

Another feature of QCD as a non-abelian gauge theory is color confinement. The strong force carrier gluon itself is also color charged. Color charged partons, namely quarks and gluons, are never detected in isolation. In experiments, only color neutral hadrons are detected. Currently, the analytic explanation of color confinement is still not yet rigorously proven. The theoretical explanation of color confinement in QCD remains one of the unsolved problem in physics.

1.2.7 Hadronization

The formation process hadrons from partons is called hadronization. Because in experiments we only measure final state hadrons, in order to study the interactions and dynamics of quarks and gluons during partonic stage from hadron spectra, we also need to understand hadronization mechanisms. However, hadronization is in general non-perturbative and cannot yet be described by first principle QCD calculations. Therefore, physicists make phenomenological models such as the Statistical Hadronization Model [8], Lund String Model [9], Quark Coalescence Model [10] to study hadronization. Figure 1-4 shows the schematics of hadronization of a beauty quark via fragmentation and coalescence process.

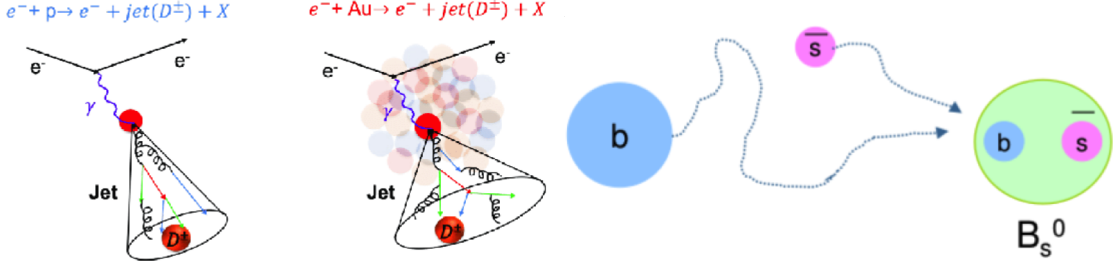


Figure 1-4: The fragmentation process of charms quarks hadronize into D^\pm (left) and the coalescence process of beauty quark with a strange quark nearby to form a B_s^0 are shown above.

1.3 QCD In Extreme Conditions

Historically, many efforts to understand QCD in extreme conditions have been made [11]. There are mainly two directions: temperature and parton density. Figure 1-5 shows the different studies of QCD in different conditions [12]:

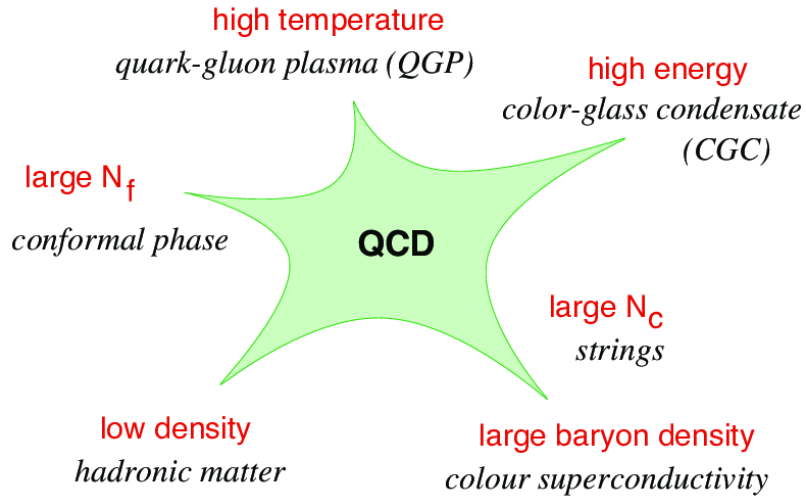


Figure 1-5: Many-body dynamics of QCD in different physics limits is shown above.

1.3.1 QCD at Finite Temperature

In QCD, under extremely high energy density, the degree of freedom of the system increases via particle production. Many-body dynamics become relevant. In the

limit of large number of quarks and gluons, after a sufficiently long period of time, the system reach thermal equilibrium via the strong interaction [13–15]. Therefore, a description based on thermodynamics can be formulated to study such systems [17]. We call this thermalized and strongly interacting many-body system of quarks and gluons to be QCD matter.

Therefore, an additional variable temperature (\mathbf{T}) can be introduced to study such QCD systems. There are some interesting QCD phenomenologies involving temperature as listed in the following subsections.

1.3.2 Melting of QCD Vacuum

The QCD vacuum is filled with various condensates of quarks-antiquark pair and gluon fields [16]. In the QCD vacuum, the three flavor of light quarks: u , d , s form a flavor symmetry group of $SU(3)_f$. However, for quark-quark pair, the $SU(3)_f \times SU(3)_f$ chiral symmetry is spontaneously broken. For example, in the vacuum, a quark-antiquark pair field has a non-vanishing expectation value of $\langle 0 | \bar{\psi}(x) \psi(x) | 0 \rangle \simeq (250 \text{ MeV})^3$ [1]. Therefore, in the physical QCD vacuum, all color field are confined in hadrons. In 1974 T.D. Lee formulated the idea that the non-perturbative vacuum condensates could be “melted down ... by distributing high energy or high nucleon density over a relatively large volume” [18, 19]. As the energy density in space increases, the color field start to permeate all space. This is effective melting the QCD Vacuum as the temperature of the system increases. Therefore, the temperature of the system will affect the QCD vacuum structure.

1.3.3 Chiral Symmetry Restoration

At a finite critical temperature $T_c > 0$, the quark-antiquark pair field will have a vanishing expectation value. In this scenario, massive quarks behave as if massless [20]. Thus, the chiral symmetry of quarks is restored [21]. Therefore, under a strong magnetic field, due to the restored chiral symmetry, the quarks generate anomalous chiral current j_5^μ described by $U(1)_A$ chiral anomaly, calculated by the famous “Triangle

Feynman diagram” in Figure 1-6 shown below:

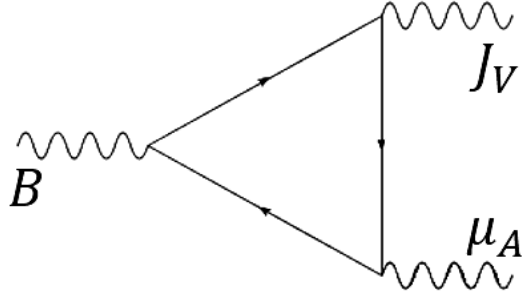


Figure 1-6: The Feynman diagram of a triangular quark loop under external magnetic field B describe the generation of chiral magnetic current via chiral anomaly is shown above.

The anomalous chiral current $j^{\mu 5}$ is given by [22]

$$\partial_\mu j_5^\mu = -\frac{N_f g^2}{16\pi^2} G_a^{\mu\nu} \widetilde{G}_{\mu\nu}^a \quad (1.6)$$

Here $G_a^{\mu\nu}$ is defined as

$$\widetilde{G}_{\mu\nu}^a = \frac{1}{2} \epsilon_{\mu\nu\lambda\sigma} G^{\lambda\sigma a} \quad (1.7)$$

According to the continuity equation of chiral current

$$\frac{\partial \rho_5}{\partial t} + \nabla \vec{j}_5 = 0 \quad (1.8)$$

By definition, the chiral current ρ_5 is the difference of the right-handed charge ρ_L and left-handed charge ρ_R .

In terms of number of particles $N_5 = \frac{Q_5}{e} = \int \rho_5 e d^3x$, integrating both sides by the spatial volume and divide by the volume, we have

$$\frac{dN_5}{dt} = \int d^3x \nabla \vec{j}_5 = \int -\frac{N_f g^2}{16e\pi^2} G_a^{\mu\nu} \widetilde{G}_{\mu\nu}^a d^3x \quad (1.9)$$

The chiral chemical potential μ_5 is proportional to the number of particle N_5 : $j_5 \propto N_5$. This non-vanishing anomalous chiral current implies non-zero chiral magnetic

dipole moment density $\mu_5 \neq 0$. Finally, under an external magnetic field, the induced electric current j_V^μ is given by

$$\vec{J}_V = \frac{N_c e}{2\pi^2} \mu_A \vec{B} \neq 0 \quad (1.10)$$

In experiments, we should expect to see the separation of left-handed and right-handed quarks Q_V due to this electric current \vec{J}_V where charge imbalance between the positive and negative direction along the magnetic field [23] as $\Delta Q = \int_0^\tau \vec{J}_V \cdot \vec{A} dt \neq 0$. We call this chirality imbalance effect due to the restored chiral symmetry of quarks at finite temperature as **Chiral Magnetic Effect** [24]. Figure 1-7 illustrates the schematics of Chiral Magnetic Effect in Heavy-Ion Collisions [25]

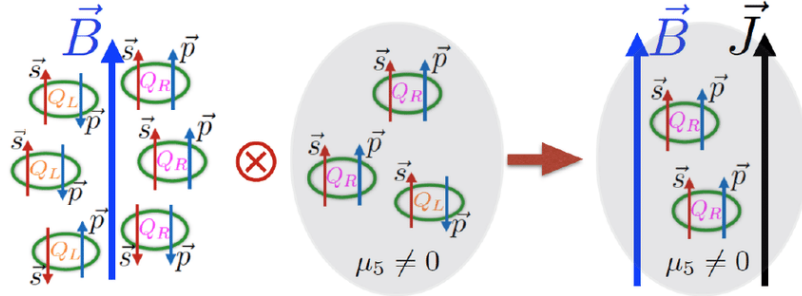


Figure 1-7: The schematics of charge separation due chirality imbalance of quarks under a strong magnetic field in heavy-ion collisions, know as Chiral Magnetic Effect, is shown above.

Currently, physicists are actively looking for evidences of Chiral Magnetic Effect in experiments but have not yet reported any conclusive results so far [26].

1.3.4 Temperature Dependence of QCD Static Potential

If we consider two color charged quarks in the limit of infinite mass and are essentially at rest in the lab frame, we can define a QCD static potential between these two quarks due to the strong interaction. In vacuum, such a potential is called “Cornell Potential” [27]. The potential as a function of the distance between two quarks is shown as follows:

$$V(r) = -\frac{\alpha_{eff}}{r} + \sigma r \quad (1.11)$$

Here, α_{eff} is the effective strong coupling between the two quarks and $\sigma \simeq 0.184 \text{ GeV}/c$ is the string coupling constant [28].

Now if we consider at finite temperature T with a thermalized system between the two quarks, the QCD static potential becomes:

$$V(r) = -\frac{\alpha_{eff}}{r} e^{-m_D r} + \frac{\sigma}{m_D} (1 - e^{-m_D r}) \quad (1.12)$$

Here, $m_D \sim g_s T$ is the Debye mass due to Debye color screening effect [29], which essentially modifies the gluon propagator by inserting a finite mass term: $-i \frac{g^{\mu\nu}}{q^2} \rightarrow -i \frac{g^{\mu\nu}}{q^2 - m_D^2}$. In fact, Equation (2) reduces to the Cornell potential when $T = 0$. The QCD static potential is shown below in Figure 1-8 [30]

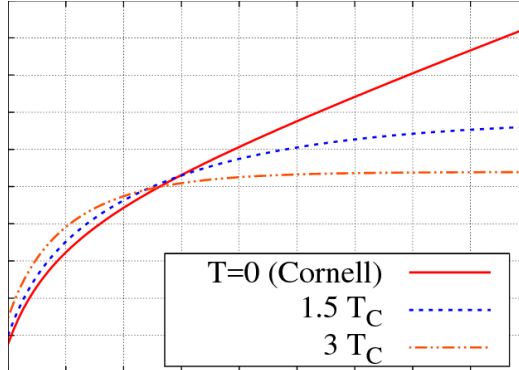


Figure 1-8: The QCD potential $V(r)$ from at zero and at finite temperatures as a function of distance r is shown above. Here, the critical temperature $T_c = 192 \text{ MeV}$. We can see that the QCD saturates at a finite value at finite temperature.

Many interesting physics implications can be derived from QCD at finite temperature.

1.3.5 Hadron Mass Spectrum and Hagedorn Temperature

In 1965, Hagedorn proposed a statistical thermodynamically bootstrap model, giving the temperature dependence of hadron spectra [31]. According to the principle of

asymptotic bootstrap, in the limit of high mass resonance $m \rightarrow \infty$ the mass spectrum of hadrons $\rho(m)$ grows exponentially

$$\rho(m) \propto m^{-\frac{5}{2}} e^{\frac{m}{T_0}} \quad (1.13)$$

Here, $\rho(m) dm$ stands for the number of excited hadron with mass between m and $m + dm$. $T_0 \simeq 158$ MeV is the temperature parameter extract from experiments. As $T \rightarrow T_0^-$, $\rho(m) \rightarrow \infty$. The mass spectrum of hadrons diverges. Therefore, it stands for the highest possible temperature achievable for the strong interaction between hadrons. Hence, T_0 is also called the “Hagedorn Temperature”. For $T > T_0$, the description of color-neutral hadrons mass spectrum will break down, indicating a new type of matter with deconfined degree of freedom in the interaction [32].

1.3.6 Color Deconfinement

As mentioned in the sections above, we see that, at finite temperature, the QCD static potential is screened and color degree of freedom become relevant in the system. As the temperature of the system increase, the quarks and gluon inside color-neutral hadrons will have more available space to move around and start to deconfine [33]. At some critical temperature T_c , quarks and gluons will form a new type color deconfined QCD matter, which is called Quark-Gluon Plasma (QGP). The typical temperature of QGP is in the order of a few hundred MeV or about 10^{12} K, which is about hundreds of thousands times hotter than the core of the Sun.

1.3.7 QCD at High Parton Density

In the other direction, while keeping zero temperature, by increasing density of the color fields of the system, another form of QCD matter will also emerge [34]. Due to confinement, a single quark or gluon cannot exit in vacuum. Therefore, the simplest form of QCD system will be a meson, which consist of one quark and one antiquark. The next more complex system will be baryon, for instances, nucleons, which consistent of three quarks. We can then use nucleons to form atomic nuclei and even

neutron stars. As the number of nucleons in the system increases, the nucleon density also increases, which increase the color field density. Below, we will discuss the consequence of increasing color field density by increasing the color field lines and decreasing the volume of the system. In general, we can study QCD at High Parton Density by probing small- x physics [35]

1.3.8 Color Glass Condensate

One way to increase the color field density is by decreasing its volume. The radius of a hadron will shrink due to the Lorentz contraction effect as it moves with respect to the spectator. However, since the number of color charges inside the does not change, the color field density will increase. According to the parton distribution function (pdf), at small x , the gluon pdf will dominate. Hence, at very high energy, which is equivalent to small x , the hadrons will turn into “gluon walls” [36] and form a dense color field of matter [37] named Color Glass Condensate (CGC) is formed [38].

1.3.9 Gluon Saturation

However, it is believed that color density of a hadron will not increase indefinitely due to gluon splitting process: $g \rightarrow gg$. At very small x , recombination of gluons: $gg \rightarrow g$ also occurs. These two processes compete and eventually balance. They result in a equilibrium color density or, equivalently, a saturation scale Q_s^2 [39]. We call this phenomenon as gluon saturation. Gluon saturation can be described by QCD evolution equations [40–44]. Figure 1-9 below shows schematically the different state of a hadron in the double-log scale plot of energy landscape $\ln x$ and the virtuality $\ln Q^2$ [45]

At the EIC, experiments will also be capable of precisely investigating gluon saturation effects through dihadron correlations analysis [46].

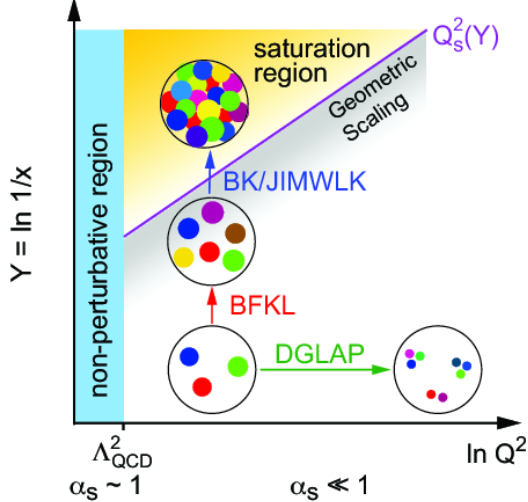


Figure 1-9: The double-log scale of energy landscape $\ln x$ and the virtuality $\ln Q^2$ diagram picturing the different regimes of the hadron wave function, the saturation line separates the dilute (DGLAP) regime from the dense (saturation) regime is shown above.

1.3.10 Nuclear Shadowing

At high energy, or equivalently, small x , according to the QCD evolution equation, the gluons inside the nucleon of the nuclei will “create shadows” on each other [47]. The high density effects results in the modification of the nuclear structure function and the gluon nucleon parton distribution [48]. Therefore, in high energy hadron-nucleus collision, we expect to see the decrease of cross section per participant nucleons at small- x region compared other x region [49]. We call this effect as “nuclear shadowing (of gluons)” [52].

1.4 QCD Matter

1.4.1 QCD Phase Diagram

Similar to form everyday matters such as metal, water, wood, glass, and plastic, which are formed by electromagnetic interaction and could all be described macroscopically by equations of states that are parameterized by thermodynamic variables. Figure 1-10 shows the phase diagram of water (H_2O) at different temperature and pressure:

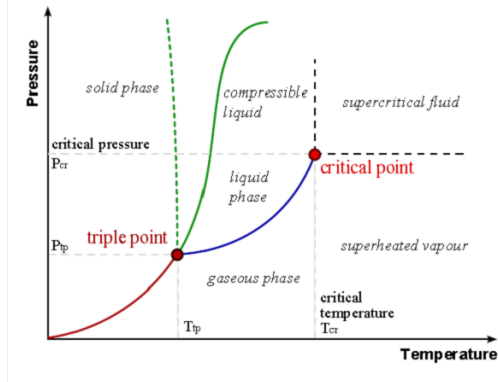


Figure 1-10: The P-T diagram of water in gas, liquid, solid phases is shown above.

Similarly, QCD matter is the matter formed by numerous quarks and gluons via the strong interaction and can also be described by equations of states. Like our everyday matter which has gas, liquid, and solid phases at different pressure and temperature, QCD matter also has different phases at different temperature and baryon chemical potential. and can be described by QCD phase diagrams. Figure 1-11 shows the QCD phase diagram at different temperature and baryon chemical potential:

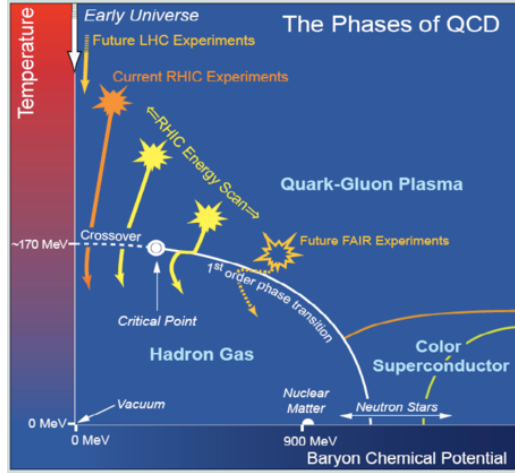


Figure 1-11: The theoretical QCD phase diagram of different QCD matter, including hadron resonance gas, quark-gluon plasma, neutron star, and color superconductor, as function of temperature and baryon chemical potential is shown above. The solid line indicates the conjecture of first order phase transition between quark-gluon plasma and hadron gas while the dash line is a smooth crossover.

1.4.2 Hadron Resonance Gas

One of the most familiar type of QCD matter is hadron resonance gas, which lies at the left bottom corner of the QCD phase diagram. Hadron resonance gas is a system of color neutral hadrons at relative low temperature. The interaction between hadrons are the Van der Waals like strong nuclear force as the residue of the color force via exchange of mesons. The strong nuclear force between two nucleons shown below Figure 1-12.

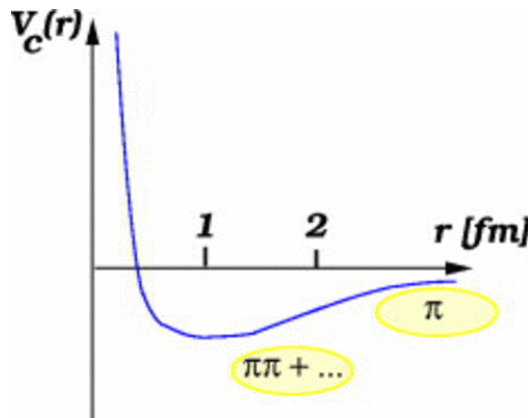


Figure 1-12: The schematic plot of potential energy between two nucleon via pion exchange as a function of distance is shown above [53]. This potential with a well minimizing near 100 MeV allow nucleons to bind together and form atomic nuclei and nuclear matter.

The equation of state of non-interacting hadron resonance gas could be described by grand canonical ensemble of bosons (mesons) and fermions (baryons) [50]. We should note that pions dominates the hadron gas at low temperature. The realistic equation of state of hadron resonance gas should also consider the interaction. An example of the equation of state of hadron resonance gas consider the Van der Waals interaction comparing with lattice QCD simulation is given in Figure 1-13 below [51]:

Nuclear matter is considered as part of the hadron resonance gas in the QCD phase diagram. Examples of typical hadron gas will be atomic nuclei at a famous nuclear matter saturation density $n_S = 0.16 \text{ fm}^{-3}$ (baryon density $n_B = 3n_S$) and nuclear matter like neutron star at large baryon density.

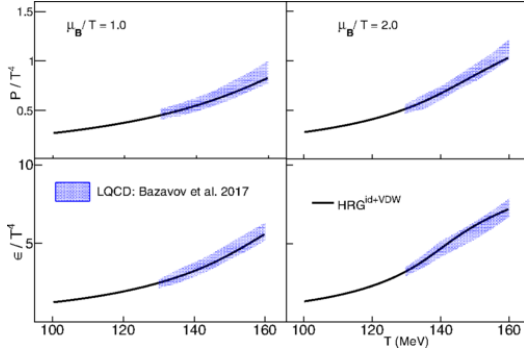


Figure 1-13: The pressure and energy density from lattice simulation compared with ideal hadron resonance gas and Van der Waas interaction at different $\frac{\mu_B}{T}$ are shown above.

1.4.3 Quark-Gluon Plasma

At very high temperature, quarks and gluons inside the color neutral hadron resonance gas will deconfine and form a new type of matter called quark-gluon plasma (QGP). In cosmology, it is believed that QGP exists in the early universe just several microseconds after the Big Bang during the quark epoch after electroweak phase transition and before nucleosynthesis [54].

The temperature of QGP is in order of hundreds of MeV, which is about hundreds of thousands times hotter than the core of the Sun. Moreover, according to extensive experimental and theoretical studies, QGP demonstrates strongly coupled ideal liquid behavior, which directly contracts to the prediction from asymptotic freedom which predict such matter should behavior like a gas of weakly interacting quarks and gluons. Therefore, the inner workings and proper degrees of freedom of QGP must be somewhere in between weakly coupled quarks and gluons and color neutral hadrons because it still demonstrate significant color freedom due to deconfinement. However, the microscopic structure of QGP is still unknown. Currently, both experimental and theoretical efforts have been conducted to actively investigate the internal structure of QGP.

Based on its ideal liquid feature, QGP could be described by relativistic viscous hydrodynamics. In fact, the quantum limit predicted by the Anti-de-Sitter Space Conform Field Theory (AdS/CFT). It is about a factor of larger than water.

The accurate equation of state of QGP is currently unknown. However, it is safe to assume that the strong interaction dominates in the QGP phase because its large coupling results in large cross section compared to the electroweak interaction cross section. Therefore, one can consider only strong interaction between quarks and gluons in the QGP. According to MIT Bag Model, the energy density ϵ and pressure p of a plasma of free quarks and gluons as a function of temperature T is as follows [55]:

$$\epsilon = \frac{37\pi^2}{30} T^4 + \mathcal{B} \quad (1.14)$$

$$p = \frac{37\pi^2}{90} T^4 - \mathcal{B} \quad (1.15)$$

Here, \mathcal{B} is the Bag Constant, which can be understood as the pressure of the vacuum on the quarks and gluons to make them form hadrons with finite size.

If we represent p in terms of ϵ , we get

$$p = \frac{1}{3}(\epsilon - 4\mathcal{B}) \quad (1.16)$$

Figure 1-14 below shows the equation of state of QGP of three flavor quarks of different model at $\mu_B = 0$ [56].

We can clearly see that a gradual rise of the pressure from near 0 to 1 as the temperature increases, indicating an smooth increase the total degree of freedom of the system due to the color deconfinement.

1.4.4 Color Superconductor

Under extremely high net baryon density, there is another hypothetical state of QCD matter named Color Superconductor where the color charges can move freely [57]. Similar to the Cooper Pair formation mechanism of electrons in metals, quarks, as fermions, pair up and bosonized into diquark, and undergo Bose-Einstein condensation [57]. The diquark condensate, carrying color charges, can move without resistance and thus demonstrate color superconductivity. It is believed that the color supercon-

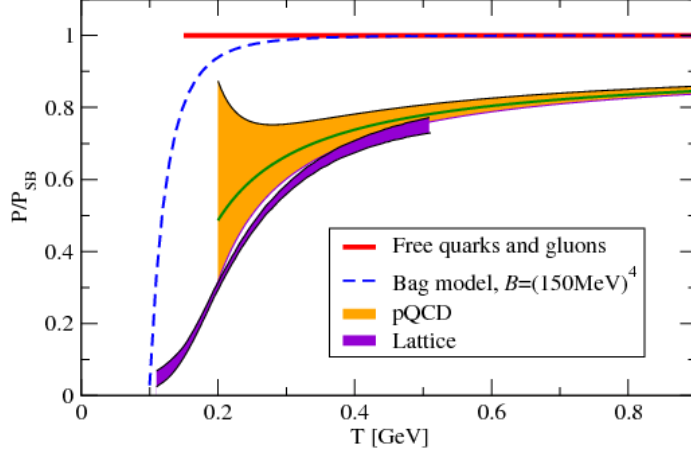


Figure 1-14: Predictions the normalized pressure to the stefan Boltzmann pressure $P_{SB} = \sigma T^4$ as a function of temperature T for three-flavor QGP obtained from lattice QCD, the MIT bag model and perturbative QCD including their uncertainties bands are shown.

ductor exists in the core of neutron stars where the net baryon chemical potential is high [58]. However, so far no color superconductor has been discovered in laboratory or astrophysical observations.

1.4.5 Phase Transition

As we increase the temperature, hadron resonance gas will undergo a phase transition into QGP. The chiral symmetry is restored from the phase transition of hadron resonance gas to QGP. However, the order of the phase transition from resonance hadron to QGP is still unknown. According to lattice QCD calculations, near zero baryon chemical potential ($\mu_B = 0$), the phase transition is a smooth cross over. According to lattice QCD calculations, at $\mu_B = 0$, the degree of freedom transition drastically increases near the critical temperature T_c .

However, at finite baryon chemical, it is believe that the phase is a first order phase transition according to different model calculations [59]. The hint of first order phase transition can be found in the softening equation of state in the cross over region [60]. However, currently, the order of phase transition from hadron resonance gas to QGP at high baryon chemical potential is still an open question.

1.4.6 Critical Point

If the theoretical predictions are correct, according to thermodynamics, there must be a critical point between the first order phase transition and the smooth crossover. Theoretical calculations predict that the critical point is $\mu_B = 350 - 700$ and $T_c \approx 160$ MeV [61]. Experimentally, the scale of the critical temperature may occur at $T_c \approx 175$ MeV from high moment analyses [62]. The research on critical point, a landmark in the QCD phase diagram, and the phase transition between QGP and hadron resonance gas are very important topics for physicists to understand the nature of QCD matters. The STAR Collaboration has carried out a Beam Energy Scan, both Phase I and II, at RHIC and plan to extend it to higher baryon chemical potential and lower temperature in the future Fixed Target Mode to search the critical point in the QCD phase diagram. However, so far efforts to search the precise locations of the critical point is still ongoing. The results are still inconclusive [?].

1.5 High Energy Nuclear Physics

Nuclear Physics is a study of atomic nuclei and their structures and interactions, which a typical energy scale ranging from MeV to GeV. High Energy Nuclear Physics is a subfield of Nuclear Physics at an energy scale on the order of GeV using heavy nuclei ($A > 56$). Its main goal is to understand the physics of QCD matter from various approaches such as collider experiments, astrophysical observations, lattice QCD computation, and theoretical modeling. In this thesis, I will focus on the research of QGP physics from the experimental approach using high energy heavy-ion colliders.

1.5.1 Laboratories

In laboratories, high energy nuclear physicists accelerate and collide heavy ions ($A > 56$) at center of mass high energy per nucleon at greater than 1 GeV to create extremely hot and dense condition and study QGP. Historically, many colliders, such as the Alternating Gradient Synchrotron (AGS) at Brookhaven National Laboratory

(BNL), in Upton, Long Island, New York and Super Proton Synchrotron (SPS) at European Center for Nuclear Research (CERN) in Meyrin, Switzerland, and GSI at Helmholtz Centre for Heavy Ion Research with both proton-proton and relativistic heavy-ion collision capabilities, have been built and established high energy nuclear physics research programs. Today, two active colliders, the RHIC at BNL and LHC at CERN, are running at different energy with various nuclei species at a wide range of impact parameters. In the future, another one collider Facility for Antiproton and Ion Research (FAIR) running at a relatively low energy and high baryon chemical potential is being constructed at Darmstadt, Germany to map the location of critical point in the QCD Phase Diagram.

In addition to collider facilities, QGP might also be studied from astrophysical observations. For instance, strange stars, a quark star made of strange quark matter, may be form from stable strangelet according to Bodmer–Witten conjecture [63] or exist in the core of neutron stars under extreme pressure and temperature. It is believed there are several potential strange stars candidates according to telescope observations and gamma ray burst analysis [64–66].

1.5.2 Relativistic Heavy Ion Collider (RHIC)

Located at BNL in Upton, Long Island, New York, United States of America, RHIC is one of the major high energy accelerator facilities and currently the highest energy collider in America. It is a circular collider with a circumference of 3.843 kilometers and can provide proton energy up to 500 GeV and gold energy up to 200 GeV [67]. It was built in 2000 in order to search for a strongly interacting hot and dense state of matter created under ultra-relativistic heavy-ion collisions, currently known as QGP, with hints from the measurement at AGS. Moreover, RHIC provides physicists with a wide range of energies and a variety of ion species from proton to deuteron and copper to uranium create different sizes of system at different temperature and baryon chemicals. In addition, taking the advantage from its highly polarization beam with high luminosity, it has a great machine capabilities for cold QCD physics. Figure 1-15 below shows a sky view of RHIC at BNL:

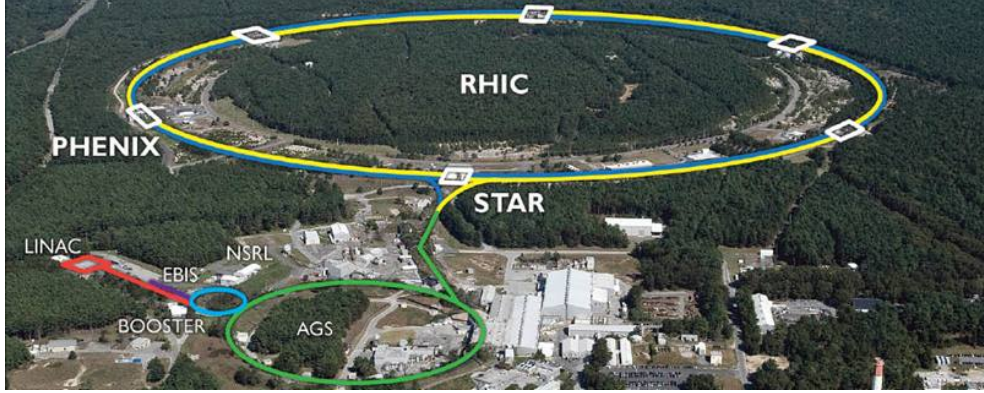


Figure 1-15: The overview of RHIC at BNL from the sky view is shown above. The actual locations of other accelerator facilities at BNL, including Linac, Booster, EBIS, NSRL, AGS, and the experiments at RHIC, STAR and PHENIX, are also labelled.

Here is how RHIC accelerates charged particles to the energy scale of GeV per nucleon. For instance, if we consider the acceleration of a typical ion source gold ($^{197}_{79}Au$) ion, we first use a cesium sputter ion source operated in the pulsed beam mode point to the gold metal and produce the Au^- ion [69]. Then, the Au^- will undergo a series of electron stripping process to reach the Au^{79+} ion [70]. First, 13 electrons are stripped by the carbon foil in the Terminal Stripping (S1) after the acceleration of tandem Van der Gaaf generator to turn Au^- to Au^{12+} . Then, the Au^{12+} ion will go through the Object Foil (S2) at the second stripping stage and becomes Au^{31+} . Next, the Au^{31+} will go through the third stripping station BTA foil (S3) made of aluminum and vitreous carbon between the Booster Synchrotron and AGS and becomes Au^{77+} . Finally, two more electrons of the gold ion Au^{77+} are removed at the fourth stripping station ATF foil (S4) made of thin tungsten, located between the AGS and RHIC. The fully stripped gold ion Au^{79+} inject to the blue and yellow rings at RHIC. For polarized protons, H^- pass a single stripping stage called located in the Booster Synchrotron. The stripping station is called Linac-to-Booster (LTB) stripper made of carbon foils with special geometry and converts polarized H^- to H^+ . Figure 1-16 schematically shows the accelerating process of gold ions at RHIC [71]

At RHIC, we will accelerate the Au^{79+} ions in the superconducting Radio Fre-

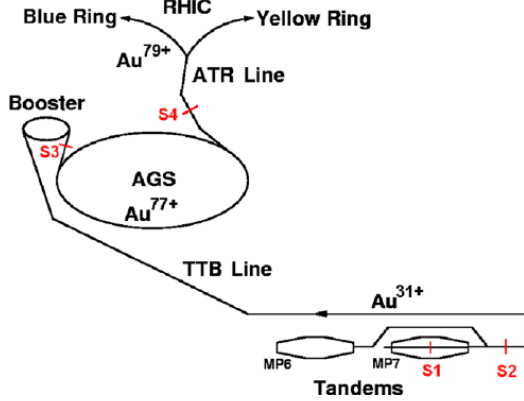


Figure 1-16: The acceleration of gold ions for RHIC is shown above.

quency (RF) cavity under perpendicular electric and magnetic fields and increase their energies to about 100 GeV/c per nucleon. Then, we collider them via bunch crossing at interaction points of the experiments to perform relativistic heavy-ion collisions to study high energy nuclear physics. The RHIC collider usually operates in the first six months of a calendar year. At RHIC, the energy can also be lower where the ion beam collides with ions at a lower energy in the laboratory frame. STAR beam energy scan even fixed target mode.

1.5.3 Large Hadron Collider (LHC)

Located at the border between Switzerland and France, LHC is one of the major high energy accelerator facilities in Europe and currently the highest energy collider in the world. It is a circular collider with a circumference of 26.7 kilometers and can provide proton energy up to 14.0 TeV and lead ion energy up to 5.02 TeV [72]. It was built in 2008 with the main purpose to discover the Higgs Boson, perform precision measurements on SM, and search for Physics beyond SM. Due to its high energy and ion capabilities, high energy nuclear physicists also use the existing general purpose detectors for high energy particle experiment at the LHC to conduct research on relativistic heavy-ion physics. LHC ion physics runs usually starts at the end of the year and lasts for about a month. The photo taken from the sky to picture LHC is shown in Figure 1-17:

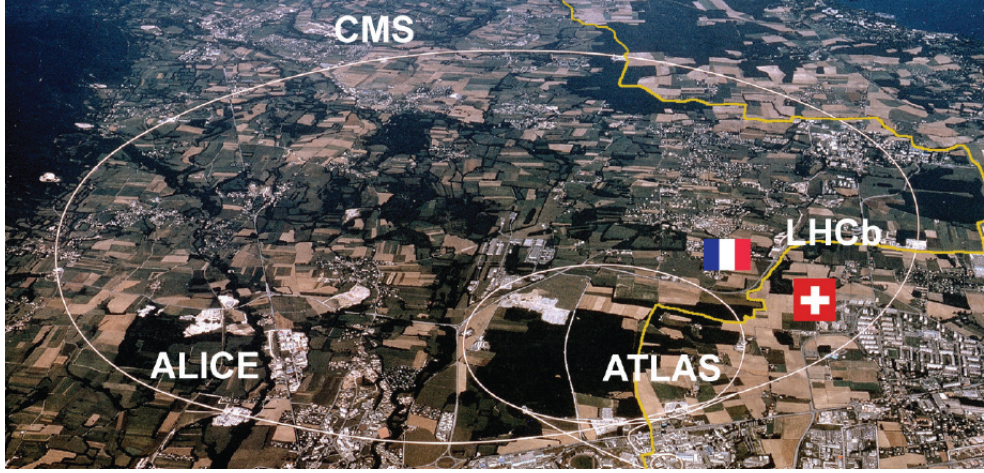


Figure 1-17: The overview of LHC at CERN from the sky view is shown above. The actual locations of the experiments at the LHC, ATLAS, CMS, ALICE and LHCb, as well as the French-Swiss border, are also labelled.

The ion source CERN usually uses is lead $^{208}_{82}Pb$, which is stable and approximately spherical. In the 2017 ion run, it also used the xenon $^{131}_{52}Xe$. Currently, there is also a discussion of potential future lighter ions such as oxygen $^{32}_{16}O$ [73]. Similar to RHIC, the lead ion at the LHC also undergoes a series of stripping processes using stripping foils in to order to become partially ionized Pb^{81+} [74]. Also, the lead ions pass a series of energy boosting before reaching to the desired energy at the LHC. Lead ions starts from a source of vaporized lead and enter Linac 3 before being collected and accelerated in the Low Energy Ion Ring (LEIR) at the energy from 4.2 MeV to 72 MeV. Then, the lead ion will inject to Proton Synchrotron (PS) to boost its energy. Then, the they are sent to the Super Proton Synchrotron (SPS). Finally, the lead ion are injected to the LHC and increase their energy to TeV scale two LHC rings with the RF cavity with 400 MeV and an electric field strength of 5 MV/m [72]. The energetic lead ions beams from two LHC rings will collide heads on with a small crossing angle at the interaction points of the LHC experiments. The CERN accelerator complex is shown schematically in 1-21

After Run III, LHC will upgrade to High Luminosity (HL) LHC and allow physicists to collect huge datasets, which is crucial for the precision measurements to study QGP in the heavy-ion physics program.

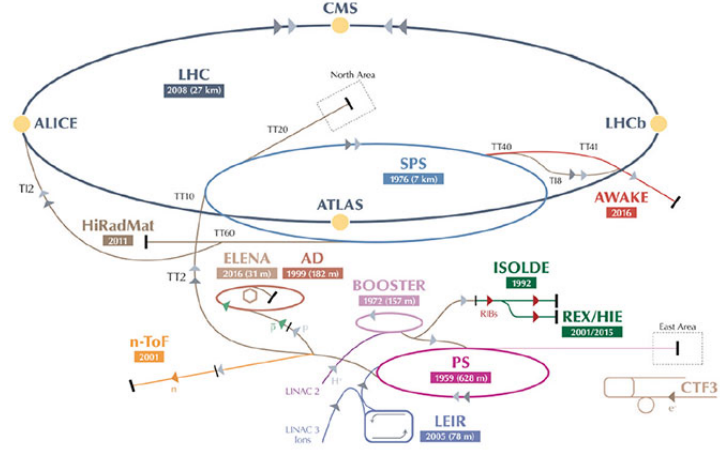


Figure 1-18: The schematic overview of CERN accelerator complex with the accelerators labelled is shown above. Proton and lead ion are accelerated using these facilities to boost to the energy scale of TeV.

1.5.4 High Energy Physics Coordinates

As mentioned in the previous section, the collision system of heavy-ion is in general highly relativistic. Therefore, Lorentz transformation will be relevant in our studies. In Cartesian coordinates $x^\mu = (t, x, y, z)$, under Lorentz transformation, if we boost the system by a speed β in the $+z$ direction. The Lorentz gamma factor will be given by $\gamma = \frac{1}{\sqrt{1-\beta^2}}$. The four vector $x^\mu \rightarrow x'^\mu$ transforms as follows

$$\begin{bmatrix} t' \\ x' \\ y' \\ z' \end{bmatrix} = \begin{bmatrix} \gamma & 0 & 0 & -\gamma\beta \\ 0 & 1 & 0 & 0 \\ 0 & 0 & 1 & 0 \\ -\gamma\beta & 0 & 0 & \gamma \end{bmatrix} \begin{bmatrix} t \\ x \\ y \\ z \end{bmatrix} \quad (1.17)$$

The equation above is called the Lorentz Transformation. It is an orthogonal transformation preserving the Minkowski metric tensor $diag(1, -1, -1, -1)$ using particle physicists conventions.

Experimentally, nowadays, heavy-ion detectors usually have 2π angular coverage in the transverse direction with some finite longitudinal acceptance along the beam

line. They look cylindrically symmetric. Hence, it is convenient and wise to choose a cylindrical coordinate system and use kinematic variables with Lorentz invariance, including boosting and rotation. In standard cylindrical coordinates in the position space, Lorentz four-vectors is used $(t, x, y, z) \rightarrow (t, r, \phi, z)$.

The relativistic coordinate system for our analysis are shown below in Figure 1-19.

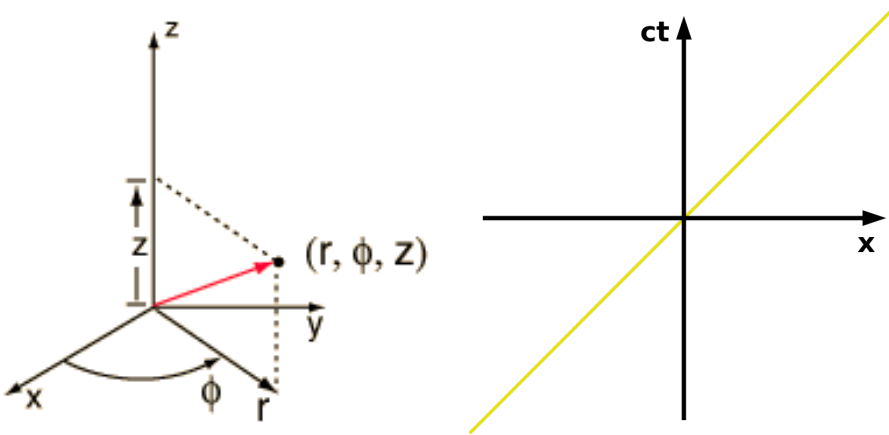


Figure 1-19: The cylindrical coordinate system in the position space (left) and the space time diagram (right) for relativistic heavy-ion physics analysis are shown above.

Thus, for the momentum space, we can use $p^\mu = (E, p_x, p_y, p_z) \rightarrow (E, p_T, \phi, p_z)$

$$p_T = \sqrt{p_x^2 + p_y^2} \quad (1.18)$$

$$\phi = \arctan\left(\frac{p_y}{p_x}\right) \quad (1.19)$$

We also define rapidity y , a relativistic version of velocity that can be convenient add to the boost.

$$y = \frac{1}{2} \ln \frac{E + p_z}{E - p_z} \quad (1.20)$$

Experimentally, we also use pseudo-rapidity η , which is more directly connected to the detector measurement assuming ultra-relativistic limit kinematics ($E \rightarrow p$). The definition of pseudo-rapidity η is shown as follows:

$$\eta = -\ln \tan\left(\frac{\theta}{2}\right) \quad (1.21)$$

Here θ is the angle labelled in the left of Figure 1-19. Particularly, $y = 0$ and $\eta = 0$ when $p_z = 0$. In addition, boosting by a speed β in the longitudinal z-direction, we found that the rapidity simply shift by a const number $y' = y + \tanh \beta$. We should note that the cylindrical coordinates (p_T, ϕ, p_z) are perfectly orthogonal while (p_T, ϕ, y) or (p_T, ϕ, η) are not.

For general collider experiments, two particles are moving toward each other with four-momenta p_1^μ and p_2^μ and interact with each other. It is also very convenient to use the Mandelstam variables s, t, u in our studies. They are defined as follows

$$s \equiv (p_1 + p_2)^2 \quad (1.22)$$

$$t \equiv (p_1 - p_2)^2 \quad (1.23)$$

$$u \equiv (p_1 - p_3)^2 \quad (1.24)$$

Here the center of mass frame, since we know the tree vector $\vec{p}_1 = -\vec{p}_2 = \vec{p}$ energy is the Mandelstam variable $s \equiv (p_1 + p_2)^2$ where p_1 and p_2 are the four-momenta of the incident beam particles. Therefore, we can see that $p_1^\mu = (E, \vec{p})$ and $p_2^\mu = (E, -\vec{p})$. Hence, $s \equiv (p_1 + p_2)^2 = 4E^2 = E_{CM}^2$. Hence, the center of mass energy of the collision system could be represented by the Mandelstam variable \sqrt{s} : $E_{CM} = \sqrt{s}$.

1.5.5 Stages of Heavy-Ion Collisions

In high energy heavy-ion collisions, both Electroweak and QCD processes occur in each event and contribute to the total cross section. We classify the events with elastic and inelastic reaction processes. For elastic processes, two nuclei scatter mainly electromagnetically with each via photon exchange without breaking themselves up or losing energy. For inelastic scattering, we classify diffractive and non-diffractive

disassociation processes. In diffractive dissociation processes, the two nuclei may be slightly excited and lose a relatively small fraction of energy, producing relatively small number of particles. On the other hand, in non-diffractive dissociation processes, the nuclei lose a substantial fraction of their energies and produce a large number of particles [75].

Therefore, in events with significant contribution from non-diffractive dissociation, the interaction between two nuclei is indeed a multi-stage process including both perturbative and non-perturbative QCD processes. We can define stages of heavy collisions and understand the details of each stage. It consists of five stages: initial state of two high Lorentz contracted nuclei before the collision, the very early pre-equilibrium stage where hard scattering between partons inside nuclei starts, the rapid expansion of the fireball begins when the thermally and chemically equilibrated QGP, the hadronization stage after QGP expands and cools down, and the freeze-out stage when the inelastic scattering process ceases.

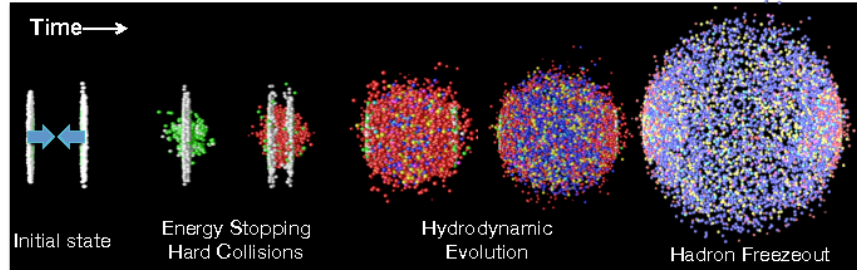


Figure 1-20: An event of a typical heavy-ion collisions event with different stages as time evolves is shown above.

Theoretically, many phenomenological models such as Ultra-Relativistic Quantum Molecular Dynamics (UrQMD) and A Multi-Phase Transport Model (AMPT) are developed to describe relativistic heavy-ion collisions.

1.5.6 Global Event Observables

Globally, we can define some physics quantities to describe heavy-ion collisions to generally characterize each event. Heavy-ion Physicists defined the impact parameter,

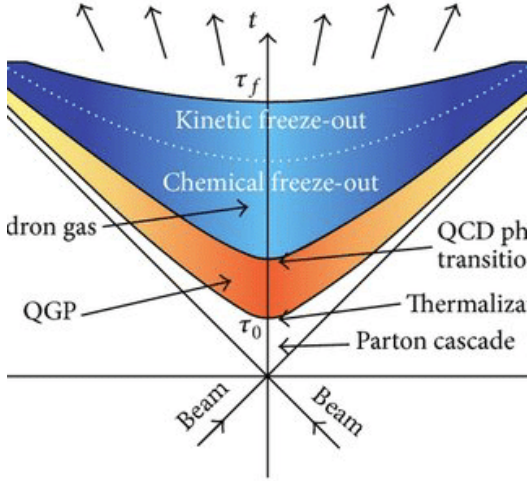


Figure 1-21: The space-time evolution of heavy-ion collisions is shown above. It consists of four stages: initial state before the collision, the creation of quark-gluon plasma right after of the collision, hadronization after quark-gluon plasma expands and cools down, and the freeze-out stage when the inelastic scattering process ceases.

centrality, number of participants, We will discuss all of them below.

Impact Parameter: Prior to heavy-ion collisions, similar to other collider experiments, each event are prepared with the same unpolarized incoming particles with the same center of mass energy. Therefore, the incoming state $|i\rangle$ is used for each event. However, different from e^+e^- and pp collision, in heavy-ion physics, we introduce another parameter called the impact parameter denoted b to the transverse distance between center of two nuclei to classify the events. Therefore, the incoming state can be rewritten as $|i(b)\rangle$. Figure 1-22 shows the definition of impact parameter in heavy-ion collision [76].

Number of Participating Nucleons: Right at the end of heavy-ion collisions after two nuclei pass through with each other, we can define the number of participating nucleon denoted N_{part} . The smaller the impact parameter, the more overlap volume between two nuclei, leading to a larger number of number of participating nucleon in the collision. The nuclear interaction system size is determined by the number of participating nucleons. However, due to event-by-event nuclei geometry fluctuations caused by the motion of nucleons inside nuclei [77], it is more proper

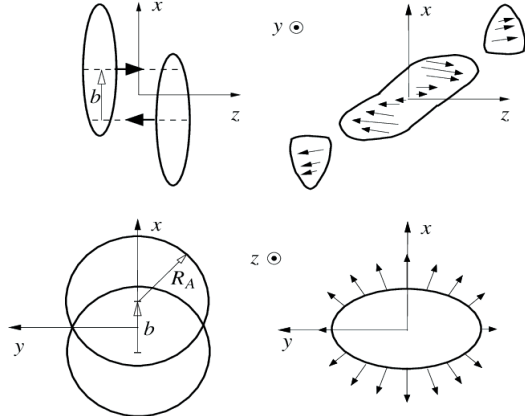


Figure 1-22: The definition of impact parameter b in heavy-ion collision and the overlapping interaction region and the break up remnants of the two nuclei, which is called spectator, moving in the z -direction are shown above. We can also see that heavy-ion collisions have an almond shape interaction region, which results in the azimuthal anisotropic emission of final state particles.

to say that the average number of participating nucleon is related to the impact parameter.

Number of Binary Nucleon-Nucleon Collisions: In addition to N_{part} , we can also define another quantity that characterize details interaction of the events at the rather hard scale. The number of binary nucleon-nucleon collisions, denoted N_{coll} , is also related to the impact parameter. At higher energy, nucleons inside nuclei become a relevant degree of freedom to the cross section. We could treat the collisions of two nuclei as the superposition of the collisions between nucleons inside the nuclei. Since binary nucleon-nucleon collision has a rather small cross section, it dominates the total nucleon-nucleon cross section according to binomial principle. Glauber model is developed to study the relationship between b , N_{part} , and N_{coll} in nuclei collisions and will be discussed in the following subsection.

Centrality: Experimentally, it is difficult to directly measure the impact parameter of each collision. Therefore, we define another physical quantity called centrality to characterize the impact parameter. The centrality (C) is defined fraction of the total nuclear interaction cross section: $C = \int_0^b \frac{d\sigma}{dx} dx$. Centrality is expressed in terms of percentage [78]. It is proportional to the quantity: $\frac{\pi b^2}{4\pi R_A^2}$ where R_A is the radius

of a nuclei defined above in Figure 1-22. When the impact parameter between two nuclei is 0, the centrality is at 0%. When the impact parameter between two nuclei is $2R_A$, the centrality is 100%. There is a relationship between the centrality and the average number of participant nucleons. Heavy-ion experimental measurements are in general presented in terms of centrality or average number of participating nucleon. Experimentally, we look at the number of tracks and activities of calorimeters at the very forward direction (Zero Degree Calorimeters) to estimate the centrality [79–81].

Virtuality: Similar to deep inelastic scattering, we can also define the virtuality Q^2 , which is the momentum transfer between the two nucleons in nucleon-nucleon collisions. To generate nucleon-nucleon collision event, we used \hat{p}_T , defined as the transverse momentum of the hard subprocess, which is a quantity related to Q^2 , developed by the high energy theory group of Lund University.

Event Multiplicity: We can also define the event multiplicity by counting the number of final state charged particles to quantify the activity of the event. Event multiplicity can be denoted as N_{trk} , number of tracks in the event, which is proportional to the number of charged particle denoted as N_{ch} . Figure 1-23 shows the correlation between the number of participating nucleons in a heavy-ion collision, their cross section and the impact parameter, defining the centrality classes [82].

The initial global parameters such as the collisions energy, impact parameter, and polarization can be treated the knobs for high energy nuclear physicists to play with in order to study relativistic heavy-ion collisions and create the strongly interacting system at different sizes with different chemical potentials and temperatures in the QCP phase diagram. Figure 1-24 shows an event display of thousands of tracks from a central Au + Au collision event at 200 GeV recorded by the Time Projection Chamber (TPC) of the STAR experiment at RHIC.

1.5.7 Glauber Model

The Glauber Model, named after Physicist Roy Glauber [83], is originally developed to address high energy scattering problem with composite particles in the optical limit where optical theorem is applicable [84, 85]. It is a model describing two composite

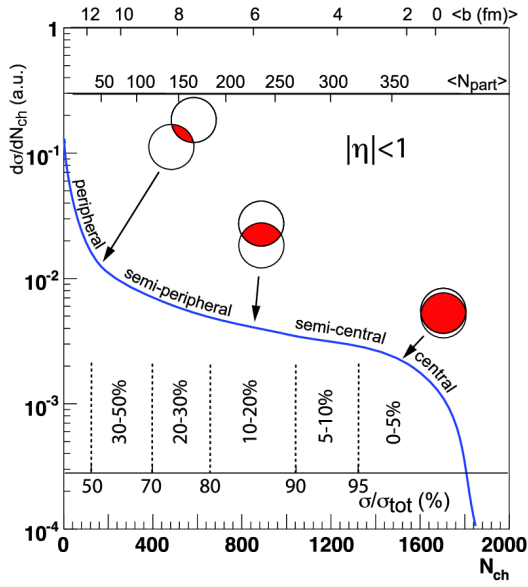


Figure 1-23: The plot showing relationship among number of charged particle, N_{ch} , related to the number of participating nucleon N_{part} , the differential cross section $\frac{d\sigma}{dN_{ch}}$, and the centrality, according to the Glauber Model calculations, is shown above.

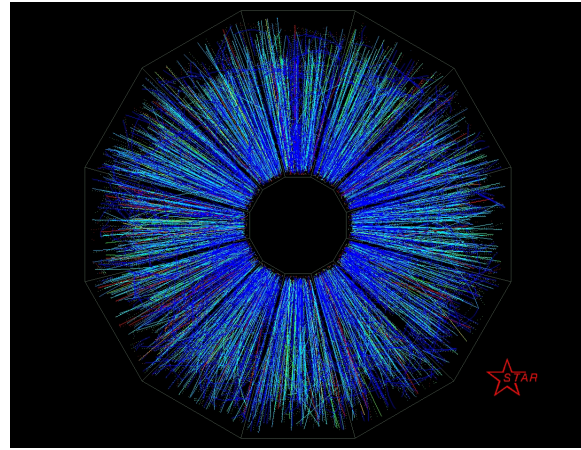


Figure 1-24: Two gold ions collide head-on in the STAR detector. The event with reconstructed tracks of final state particles are display by STAR TPC shown above.

objects collider inelastically with each other and relate the cross section to the cross section of collision between two point objects. The Glauber Model can be applied to study nucleon-nucleus (N-A) and nucleus-nucleus (A-B) collisions with nucleon-nucleon (N-N) collisions and determine relationship between the global observables mentioned in the previous subsection.

If we consider a spherically symmetric nucleus, the nuclear charge density can be parameterize $\rho(r)$ by the Fermi distribution with three parameters below

$$\rho(r) = \rho_0 \frac{1 + w(r/R)^2}{1 + \exp(\frac{r-R}{a})} \quad (1.25)$$

According to the Glauber Model [83], the N-N inelastic cross section is denoted as σ_{in}^{NN} and the effective thickness function of a nucleon is defined as a function of impact parameter in the transverse direction: $T(\vec{b})$. It is defined as follow

$$T(\vec{b}) = \int \rho(\vec{b}, z) dz \quad (1.26)$$

It is normalized to unity: $\int_0^{R_A} T(\vec{b}) d^2b = 1$. $T(\vec{b})$ essentially depends on density of the nucleus $r(b)$. If the nucleus has a uniform cylinder and the collide on its circular face along its height, then $T(\vec{b})$ will be a constant. Therefore, the probability that a nucleon collides with a nucleon inside the nucleus is given by $\sigma_{in} T(\vec{b})$. Therefore, the probability of n nucleon collision is given by

$$P_n = \binom{A}{n} \sigma_{in}^{NN} T(\vec{b})^n [1 - \sigma_{in} T(\vec{b})]^{A-n} \quad (1.27)$$

Hence, if we consider a constant fraction of μ ($0 \leq \mu \leq 1$) of particle produced after each collisions, we can calculation the average multiplicity $\langle N(\mu) \rangle$:

$$\langle N(\mu) \rangle = \sum_n P_n \sum_0^{n-1} \mu^m = \sum_{n-1} P_n \frac{1 - \mu^n}{1 - \mu} = \frac{1}{1 - \mu} \{1 - [1 - (1 - \mu) \sigma_{in} T(\vec{b})]^A\} \quad (1.28)$$

It turns out that we have the following relationship between N_{part} and N_{coll} with $\langle N(\mu) \rangle$ [83]

$$N_{part} = \langle N(\mu = 0) \rangle \quad (1.29)$$

$$N_{coll} = \frac{1}{2} \langle N(\mu = 1) \rangle = AT(\vec{b})\sigma_{in}^{NN} \quad (1.30)$$

In a more generalized case: A-B collisions, Figure 1-25 shows sides view and beam-line view of heavy-ion collision of projectile B on target A

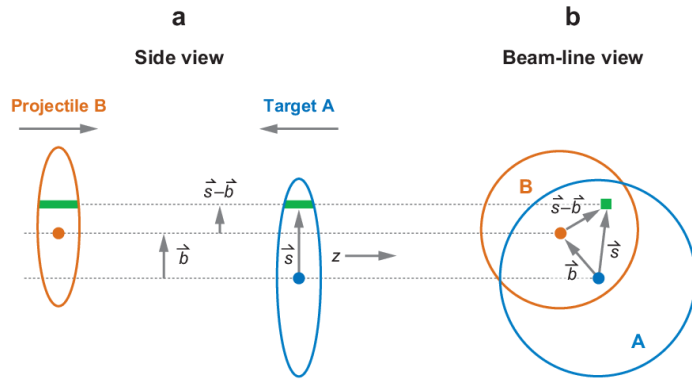


Figure 1-25: The A-B collision with the definition of the impact parameter vector \vec{b} and the distance of nucleon to the center of projectile B \vec{s} are shown above. The distance of the nucleon in B to center of the target A is $\vec{s} - \vec{b}$ according to vector subtraction rule. Here we assume both nuclei A and B are perfect spheres.

Using similar ideas [82], we could first calculate the effective thickness function T_{AB} as follows:

$$T_{AB}(\vec{b}) = \int T_A(\vec{s})T_B(\vec{b} - \vec{s})d^2s \quad (1.31)$$

Now replacing $T(\vec{b})$ in N-A by $T_{AB}(\vec{b})$ in A-B, we can obtain

$$\langle N(\mu) \rangle = \frac{A}{1-\mu} \int_0^b T_A(\vec{s}) \{1 - [1 - (1-\mu)T_B(\vec{b}-\vec{s})\sigma_{in}^{NN}]\}^A d^2s + \frac{B}{1-\mu} \int_0^b T_B(\vec{s}) \{1 - [1 - (1-\mu)T_A(\vec{b}-\vec{s})\sigma_{in}^{NN}]\}^B d^2s \quad (1.32)$$

To obtain N_{part} , evaluate at $\mu = 0$, we get

$$N_{part} = A \int_0^b T_A(\vec{s}) \{1 - [1 - T_B(\vec{b} - \vec{s})\sigma_{in}^{NN}]^A\} d^2 s + B \int_0^b T_B(\vec{s}) \{1 - [1 - T_A(\vec{b} - \vec{s})\sigma_{in}^{NN}]^B\} d^2 s \quad (1.33)$$

To obtain N_{coll} , evaluate at $\mu = 1$, we get

$$N_{coll} = AB T_{AB}(\vec{b}) \sigma_{in}^{NN} \quad (1.34)$$

In a very special case, assume the nucleon are simply perfect rigid sphere with the same radius and head-on collide with each other (impact parameter is $b = 0$). That is $T_A \sigma_{in}^{NN} = T_B \sigma_{in}^{NN} = T_{AB} \sigma_{in}^{NN} = 1$, we get

$$N_{part} = A + B \quad (1.35)$$

$$N_{coll} = AB \quad (1.36)$$

The results above of N_{part} and N_{coll} agree to our expectation.

The comparison of the Glauber Model with simulations of the N_{part} and N_{coll} as a function of impact parameter b . Figure 1-26 from the [82]

Therefore, we can apply the Glauber model to determine N_{part} and N_{coll} for a given centrality range of AA collision ($T_{AB} \rightarrow T_{AA}$), which will be used in our analysis to obtain the corrected yield. It is believed that the production of light hadrons, such as pions and kaons, are scaled as N_{part} [86] while electroweak bosons, such as W and Z boson, are scaled as N_{coll} [87].

1.6 Characterization of Quark-Gluon Plasma

Equipped with the knowledge and collider technologies of heavy-ion collisions, we are ready to apply them to conduct scientific research on QGP in laboratories. The following subsections will describe the characterization of QGP from its predicted signature to open questions today, which leads to my thesis research.

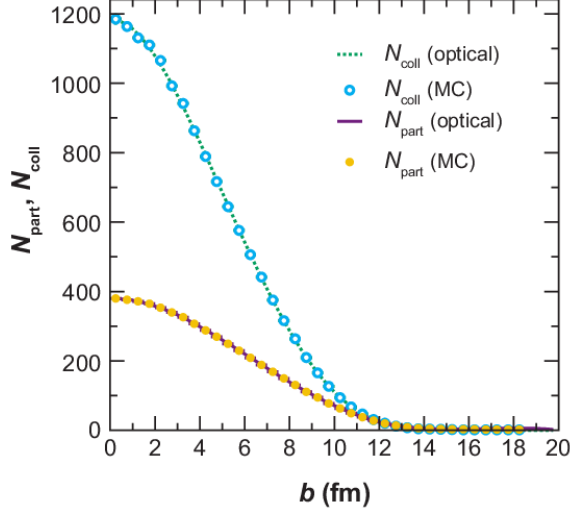


Figure 1-26: The N_{part} and N_{coll} as a function impact parameter calculated from the Glauber Model with optical approximation (lines) and from MC simulations (circles) are shown above. We can see they have almost perfect agreement with each other.

1.6.1 Signatures

QGP has been hypothesize long before its discovery as a color deconfined phase of quark matter named “quark gluon plasma” [88] and will demonstrate some specific benchmarks in experiments to prove the creation of QGP [89]. Here, four classic signatures of QGP will be discussed: J/ψ suppression, jet quenching, elliptic flow, strangeness enhancement.

J/ψ and Υ suppression: J/ψ meson, as a type of heavy quarkonia, is bound state of $c\bar{c}$, made of charm quark and an anti-charm quark, whose mass is heavier than the Λ_{QCD} . Therefore, we could approximately treat the interaction between charm and the anti-charm quark a static the Cornell potential $V(r)$ in the non-relativistic quantum mechanical hamiltonian system [90]:

$$\hat{H} = \hat{T} + \hat{V} \quad (1.37)$$

$$\hat{H} |\psi\rangle = i \frac{\partial}{\partial t} |\psi\rangle \quad (1.38)$$

and solve Schrodinger equation the to describe J/ψ mesons in vacuum [1]. As

we have seen in Section 1.3.4, with the QGP medium, at a finite temperature T , the potential is modified due to color screen effect. As the distance between two charm quarks $V(r) \rightarrow \frac{\sigma}{m_D}$, which does not diverge, as $r \rightarrow \infty$. Therefore, the $c\bar{c}$ system could be unbounded if they have sufficient energy. In the field theory picture, this could be understood as the color string breaking between charm and anti-charm quark [92], also known as quarkonia melting [93]. Hence, with the influence of QGP at $T > 0$, the production cross section of J/ψ will decrease compared to the vacuum at $T = 0$. Experimentally, we define an observable to quantify the modification of particle production cross section in AA collision compared to the reference pp collisions normalized by the number of binary nucleon-nucleon collisions N_{coll} , which is defined in the previous subsection. We called this observable as nuclear modification factor denoted R_{AA} . Mathematically, R_{AA} is defined as follows:

$$R_{AA} = \frac{1}{N_{coll}} \frac{\frac{d^2 N_{AA}}{dp_T dy}}{\frac{d^2 N_{pp}}{dp_T dy}} = \frac{1}{T_{AA}} \frac{\frac{d^2 N_{AA}}{dp_T dy}}{\frac{d^2 \sigma_{pp}}{dp_T dy}} \quad (1.39)$$

Therefore, $R_{AA} < 1$ means suppression. $R_{AA} = 1$ means no modification. $R_{AA} > 1$ means enhancement. Hence, in experiments, we should observe the $R_{AA} < 1$ a suppression of J/ψ production. Figure 1-27 shows the measurement of fully reconstructed J/ψ at RHIC and LHC [94]

In fact, we could see that $R_{AA} < 1$ for every data point, which indicates a clear suppression of J/ψ production from experiments at both RHIC and the LHC. However, we should note that the larger J/ψ R_{AA} observed at the LHC compared to RHIC could be explained by regeneration mechanism [95]. The observation of J/ψ suppression is one of the earliest evidence of the discovery of QGP.

Similarly, we expect to see this in Υ , which is made of $b\bar{b}$. Indeed, they expect to have sequential suppression since we have 3 Υ states: $\Upsilon(1S)$, $\Upsilon(2S)$, and $\Upsilon(3S)$ could be observed in experiments. Because the energy of the $b\bar{b}$ system or equivalently the rest mass: $m_{\Upsilon(3S)} > m_{\Upsilon(2S)} > m_{\Upsilon(1S)}$, a sequential suppression: $R_{AA}^{\Upsilon(1S)} > R_{AA}^{\Upsilon(2S)} > R_{AA}^{\Upsilon(3S)}$ should be observed if QGP is created. Figure 1-28 shows the measurement of fully reconstructed Υ states at RHIC and LHC [96, 97]

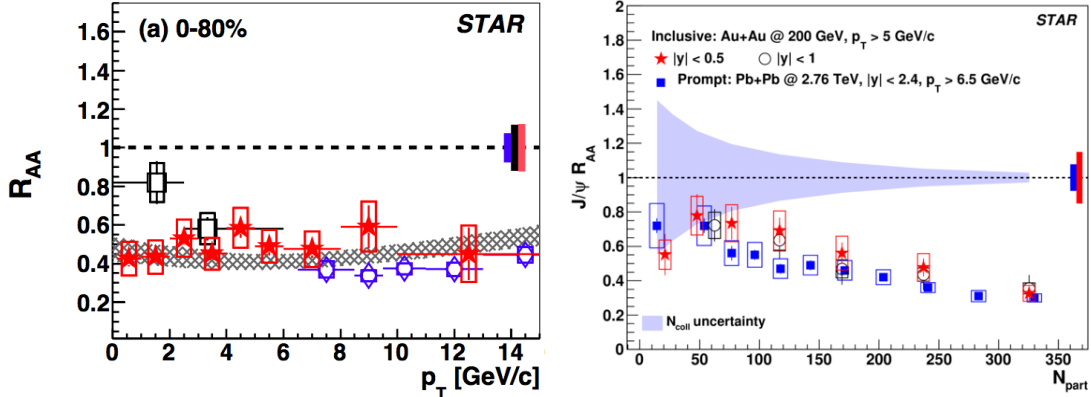


Figure 1-27: The nuclear modifications factor R_{AA} of fully reconstructed J/ψ as a function of p_T (left) and N_{part} (right) measured by the STAR experiment (red data points) at RHIC and CMS (blue diamond data points) and the ALICE (blue circle data points) experiment at the LHC are shown above. We can see that the $J/\psi R_{AA}$ is below 1 for both p_T and N_{part} . There is no significant p_T dependence of $J/\psi R_{AA}$. The $J/\psi R_{AA}$ decreases as N_{part} increases, consistent to the increasing creation probability of QGP with larger N_{part} .

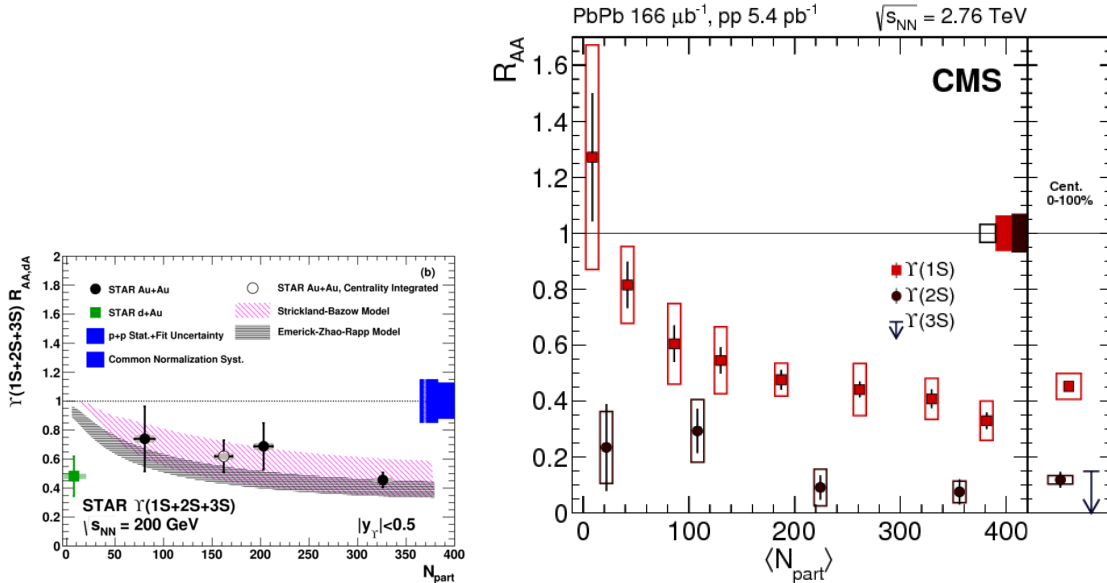


Figure 1-28: The nuclear modifications factor R_{AA} of fully reconstructed Υ as a function of N_{part} measured by the STAR experiment (left) at RHIC and CMS experiment (right) at the LHC are shown above. We can see that R_{AA} of the three Υ states is below 1 for both $N_{part} > 3$. The $J/\psi R_{AA}$ decreases as N_{part} increases, consistent to the increasing creation probability of QGP with larger N_{part} . In addition, a sequential suppression of ΥR_{AA} is observed by the CMS experiment: $R_{AA}^{\Upsilon(1S)} > R_{AA}^{\Upsilon(2S)} > R_{AA}^{\Upsilon(3S)}$, which agrees with the expectation QGP color screening effect.

Jet Quenching: Experimentally, due to color confinement, it is impossible to directly detect and track the energetic parton. Therefore, physicists define jet as a spray of collimated hadrons within a narrow cone initiated from the color charged parton. In nuclear and particle physics, jets are used to study the dynamics of partons before hadronization [98] and understand the properties of QGP [1]. A schematic view of a di-jet production from di-quark event in electron-positron collider $e^+e^- \rightarrow q\bar{q}$ is shown below in Figure 1-29

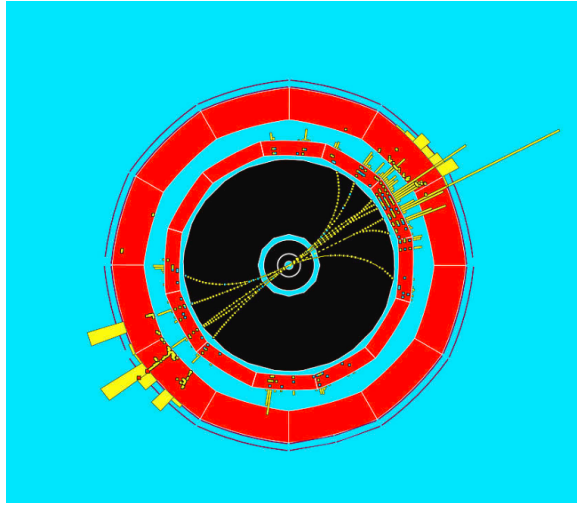


Figure 1-29: The schematic view of a di-jet event from the ALEPH (a particle detector at the Large Electron-Positron collider) Experiment at the Large Electron-Positron Collider (LEP) is shown above. We can see two sprays of back to back particles within narrow cone, representing a di-jet event.

Since we know QGP a color deconfined phase of matter, an energetic parton carrying color charge traveling through the QGP medium is expected to lose a substantial amount its energy to the medium. This is similar the effect that an electron beam losing energy in the electron-ion plasma via electromagnetic interaction [1]. We call this effect as jet quenching. Figure 1-30 shows jet quenching in QGP in AA collisions compared to pp collisions

Experimentally, compared to pp collision where QGP is not expected to be created, the jet spectra is modified by the QGP medium. The angular distributions would be broaden due to interaction with the medium and the p_T spectra will be shifted to the

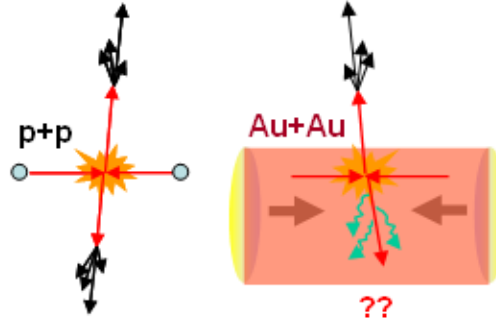


Figure 1-30: The schematic picture explaining jet quenching is shown above. Hard scatterings in pp collisions produce back-to-back "jets" of particles, but in AuAu collisions, the presence QGP modifies the jets' properties.

left due to energy loss. This can be quantified by jet nuclear modification factor R_{AA} similar to the R_{AA} for quarkonium suppression mentioned in the previously. Figure 1-31 Shows the hadron angular correlation with the STAR experiment at RHIC and jet R_{AA} as a function of p_T with the ALICE experiments at LHC [99, 100]:

The jet R_{AA} are all below 1 at RHIC and LHC, which suggest jet quenching in AA collisions, supporting existence of QGP.

Elliptic Flow: The reaction region in heavy-ion collisions, where the two nuclei overlap with each other, has an almond shape, which is azimuthally asymmetric. If a color deconfined matter QGP is created, particles emitted from the almond shape fire ball are expected to be anisotropic due to differences of the pressure gradient of the QGP in the and their path length through QGP in the x and y direction. Experimentally, physicists Dr. Arthur Poskanzer who sadly just passed away in June 30 2021, and Dr. Sergey Voloshin developed the event plane method to analyze the azimuthal anisotropy of particle emission in heavy-ion collisions [103]. The reaction plane is defined as the plane of the impact parameter and the x-axis. Figure 1-32 schematically shows the definition of reaction plane in heavy-ion collisions.

The particle spectra in heavy-ion collisions can be factorized as

$$E \frac{d^3N}{d^3p} = E \frac{1}{2\pi p_T} \frac{d^3N}{dp_T dy d\phi} = E \frac{1}{2\pi p_T} \frac{d^2N_1}{dp_T dy} \frac{dN_2}{d\phi} \quad (1.40)$$

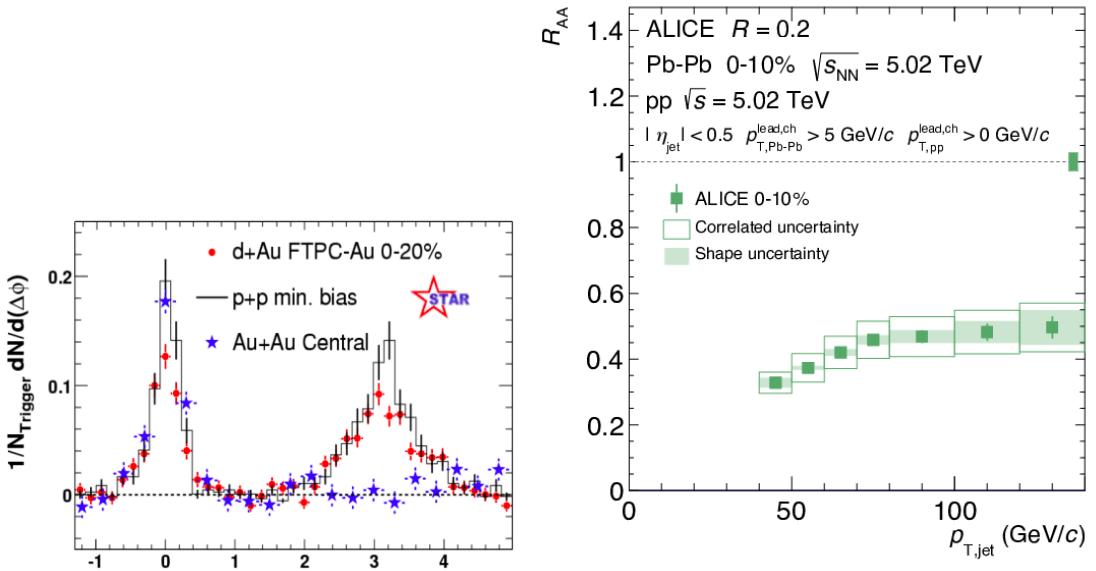


Figure 1-31: Comparison of two-particle azimuthal distributions for central dAu collisions to those seen in pp and central AuAu collisions measured with the STAR experiment jet R_{AA} as a function p_T measured by the ALICE experiment at LHC (right). From the STAR result, in central AuAu collisions, the back-to-back peak has disappeared due to the transfer of jet energy to the slow expanding medium constituents. The jet R_{AA} from ALICE measurement is clearly below 1, suggesting jet losing a significant fragment of its energy in AA collision compared to pp.

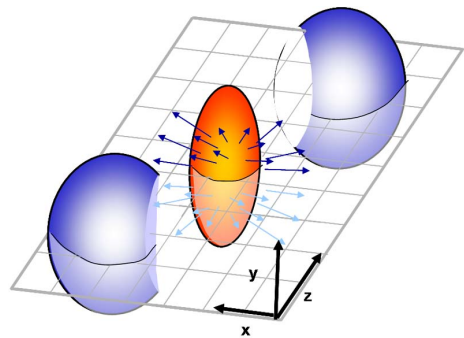


Figure 1-32: The figure above shows the ellipsoid of the overlapping nuclear reaction region of two nuclei in heavy-ion collisions. The reaction plane, which is the x-z plane shown as above, is constructed by the beam direction and the impact parameter vector. The emissions of particles are azimuthally anisotropic in the x-y plane.

Since the particle emission is azimuthally anisotropic, we can expand the $F(p_T, \phi, y) = \frac{dN_2}{d\phi}$ into a Fourier series [103]:

$$F(p_T, \phi, y) = \frac{x_0(p_T, y)}{2\pi} + \sum_{n=1}^{\infty} [x_n(p_T, y) \cos(n\phi) + y_n(p_T, y) \sin(n\phi)] \quad (1.41)$$

According to trigonometry, we get

$$F(p_T, \phi, y) = \frac{x_0(p_T, y)}{2\pi} + \sum_{n=1}^{\infty} 2v_n(p_T, y) \cos[n(\phi - \Psi_n)] \quad (1.42)$$

Here, $v_n = \frac{1}{2} \sqrt{x_n^2 + y_n^2}$ and $\Psi_n = \frac{1}{n} \arctan\left(\frac{y_n}{x_n}\right)$.

To find the Fourier coefficients v_n , we can apply the Fourier tricks to find x_n and y_n .

Theoretically, because the function $\frac{dN_2(\phi)}{d\phi}$ is continuously analytical, we can use integral to find the Fourier coefficients [18]

$$x_n = 2 \int_0^{2\pi} \frac{dN_2(\phi)}{d\phi} \cos(n\phi) d\phi \quad (1.43)$$

$$y_n = 2 \int_0^{2\pi} \frac{dN_2(\phi)}{d\phi} \sin(n\phi) d\phi \quad (1.44)$$

Experimentally, because our data take on discrete values, we can convert the integral into a sum

$$x_n = \frac{2}{N} \sum_{n=1}^N \cos(n\phi) d\phi = 2\langle \cos n\phi \rangle \quad (1.45)$$

$$y_n = \frac{2}{N} \sum_{n=1}^N \sin(n\phi) d\phi = 2\langle \sin n\phi \rangle \quad (1.46)$$

Here, we sum up all tracks in the experiment to get the x_n and y_n . Then, we will be able to find

$$v_n = \frac{1}{2} \sqrt{x_n^2 + y_n^2} = \sqrt{(\langle \cos n\phi \rangle)^2 + (\langle \sin n\phi \rangle)^2}. \quad (1.47)$$

In heavy-ion physics, the first order Fourier coefficient v_1 is called the directed

flow.

$$v_1 = \sqrt{(\langle \cos \phi \rangle)^2 + (\langle \sin \phi \rangle)^2}. \quad (1.48)$$

It can be connected to the initial tilting source of the colliding nuclei [101] and can be used to study Chiral Magnetic Effect [102].

The second order Fourier coefficient v_2 is called elliptic flow.

$$v_2 = \sqrt{(\langle \cos 2\phi \rangle)^2 + (\langle \sin 2\phi \rangle)^2} = \sqrt{(\langle \cos^2 \phi \rangle - \langle \sin^2 \phi \rangle)^2 + (2\langle \sin \phi \rangle \langle \cos \phi \rangle)^2}. \quad (1.49)$$

Assuming in initial stage before the collision, the sum of the momentum of two colliding nuclei \vec{p}_1 and \vec{p}_2 is exactly 0 without any fluctuation. That is

$$\vec{p}_1 + \vec{p}_2 = 0 \quad (1.50)$$

According to momentum conservation, for the final state particles, we have

$$\sum_i^N p_x^i = 0 \quad (1.51)$$

$$\sum_i^N p_y^i = 0 \quad (1.52)$$

Therefore, we have

$$\langle p_T \cos \phi \rangle = \langle p_x \rangle = \frac{1}{N} \sum_i^N p_x^i = 0 \quad (1.53)$$

$$\langle p_T \sin \phi \rangle = \langle p_y \rangle = \frac{1}{N} \sum_i^N p_y^i = 0 \quad (1.54)$$

But since the p_T and ϕ are completely orthogonal, the random variable p_T is uncorrected to ϕ . Therefore, we have

$$\langle p_T \cos \phi \rangle = \langle p_T \rangle \langle \cos \phi \rangle = 0 \quad (1.55)$$

$$\langle p_T \sin \phi \rangle = \langle p_T \rangle \langle \sin \phi \rangle = 0 \quad (1.56)$$

Finally, we know that $p_T > 0$, thus

$$\langle p_T \rangle > 0 \quad (1.57)$$

Hence,

$$\langle \cos \phi \rangle = 0 \quad (1.58)$$

$$\langle \sin \phi \rangle = 0 \quad (1.59)$$

Therefore, we have

$$v_2 = \sqrt{(\langle \cos^2 \phi \rangle - \langle \sin^2 \phi \rangle)^2 + (2\langle \sin \phi \rangle \langle \cos \phi \rangle)^2} = \langle \cos^2 \phi \rangle - \langle \sin^2 \phi \rangle. \quad (1.60)$$

In terms of momentum p_x and p_y , we can rewrite v_2 as

$$v_2 = \langle \cos^2 \phi \rangle - \langle \sin^2 \phi \rangle = \left\langle \frac{p_x^2}{p_T^2} \right\rangle - \left\langle \frac{p_y^2}{p_T^2} \right\rangle = \left\langle \frac{p_x^2 - p_y^2}{p_T^2} \right\rangle = \left\langle \frac{p_x^2 - p_y^2}{p_x^2 + p_y^2} \right\rangle. \quad (1.61)$$

Classically, we know that the momentum is proportional to the pressure gradient. Schematically, we could write

$$p_x \simeq \frac{m\tau}{\rho} \frac{\partial P}{\partial x} \simeq \frac{m\tau}{\rho} \frac{P}{L_x} \quad (1.62)$$

Where m is the mass of the particle, τ is the life time of the QGP, ρ is the density of the QGP, and L_x is the minor axis of the ellipse in the x direction according to the

geometry of Figure 1-32.

Likewise, we have the same relation for p_y

$$p_y \simeq \frac{m\tau}{\rho} \frac{\partial P}{\partial y} \simeq \frac{m\tau}{\rho} \frac{P}{L_y} \quad (1.63)$$

Here, L_y is the major axis of the ellipse in the y direction according to the geometry of Figure 1-32. Apparently, $L_y > L_x$.

Hence, we can write v_2 as

$$v_2 = \left\langle \frac{p_x^2 - p_y^2}{p_x^2 + p_y^2} \right\rangle = \frac{\frac{1}{L_x^2} - \frac{1}{L_y^2}}{\frac{1}{L_x^2} + \frac{1}{L_y^2}} = \frac{L_y^2 - L_x^2}{L_x^2 + L_y^2} > 0 \quad (1.64)$$

In heavy ion collision, we define the eccentricity ϵ_s of an ellipse is defined as [104]

$$\epsilon_s \equiv \frac{L_y^2 - L_x^2}{L_x^2 + L_y^2} \quad (1.65)$$

Hence, we have

$$v_2 \simeq \epsilon_s \quad (1.66)$$

Therefore, we can see that v_2 is essentially proportional to the eccentricity simply based on ellipse geometry of reaction region. Historically, v_2 has extensively studied experimentally and theoretically. It turns out the elliptic flow v_2 could be calculated using relativistic viscous hydrodynamics, which we will describe in the next section. If QGP is created, we expect v_2 of the light flavor hadrons created direction from the QGP to be positive as we derive above. Figure 1-33 show the v_2 as a function of p_T of charged light flavor hadrons in heavy-ion collisions at mid-rapidity measured by RHIC and LHC experiment [105, 106]

We can clearly see positive v_2 of charged particles at both RHIC and LHC, which also supports the creation of QGP in high energy heavy-ion collisions.

Strangeness Enhancement: As described in Section 1.4.6, the temperature of QGP is well above 100 MeV, which is much larger than the strange quark mass (about 95 MeV). Therefore, since $T_{QGP} > m_s$, in thermally and chemically equilibrated

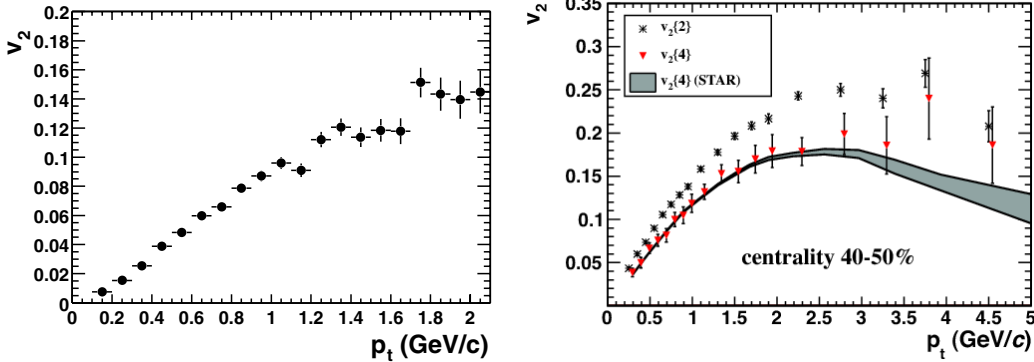


Figure 1-33: The elliptic flow of charged particles v_2 as a function of p_T in AuAu collision measured by the STAR experiments at RHIC (left) and in PbPb collisions by the ALICE experiments at LHC (right) are shown above. Clearly, $v_2 > 0$ is observed in both experiments.

QGP, strange quarks could be produced thermally via the pair production process $u\bar{u}, d\bar{d} \rightarrow s\bar{s} gg \rightarrow s\bar{s}$, creating the chemical abundance equilibrium [?]. Therefore, the strangeness content in the QGP is enhanced, which could be experimentally observed from enhancement of strange particle yields in AA collisions compared to pp collisions. A direct experimental observable is the ratio of strange hadron yield to pions in AA and pp collisions. Figure 1-34 shows measurements on strange meson and baryons to pion ratios in AA and pp at RHIC and LHC

We can see that ϕ/π ratio increases as N_{part} and \sqrt{s}_{NN} increases, which indicates strangeness enhancement in AA collisions compare to pp collisions. This again can be served as an evidence for the formation of QGP in heavy-ion collisions at RHIC and LHC.

1.6.2 Discovery

Knowing signatures of QGP, physicists build experiments in heavy-ion colliders to search for QGP. Historically, in a special seminar at CERN February 2000, the discovery of QGP was announced [111]. Figure 1-35 shows the announcement

In the U.S., after the runs of RHIC, experiments have collected enough luminosity of the dataset to perform measurements. In QM, clear signatures of QGP from the

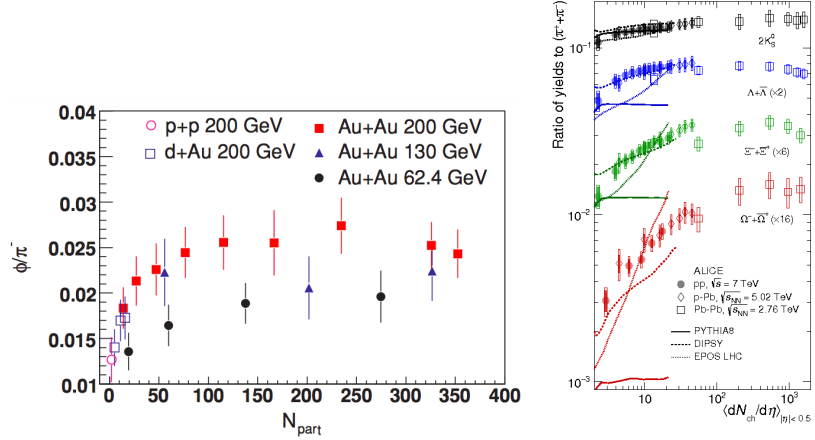


Figure 1-34: The yield ratio of ϕ/π as a function N_{part} in $p + p$, $p + \text{Au}$, and $\text{Au} + \text{Au}$ from the STAR experiment at RHIC (left) and strange hadrons $K_s^0, \Lambda^+, \Xi^0, \Omega^-$ as a function of $dN_c h/d\eta$ from the ALICE experiment at LHC are shown above. We can see a clear trend of the increase of the strange hadron to pion ratio as the event multiplicity increases. In addition, we also see that the ϕ/π ratio increases as \sqrt{s}_{NN} increases, which suggests the strangeness content enhances as the temperature of the system increase.

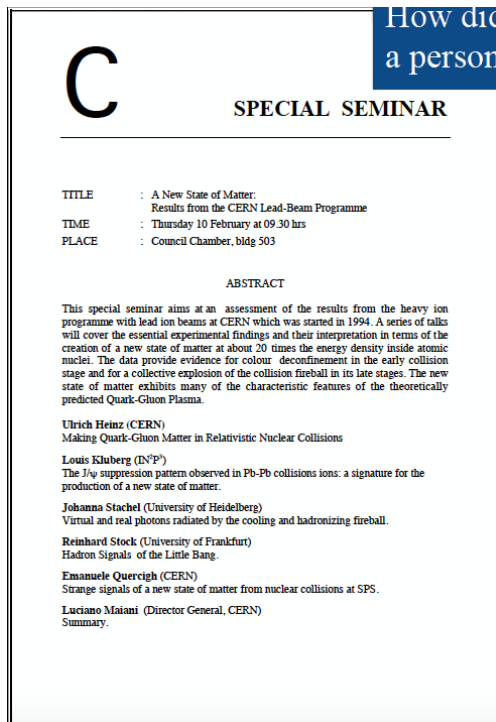


Figure 1-35: The announcement of discover of QGP in a special seminar at CERN on February 10 2000 is shown above.

measurements of with STAR, PHENIX, BRAHMS, and PHOBOS experiments have been present to the public and all support the creation of QGP. Figure 1-36 show the results presented in QM 2002.

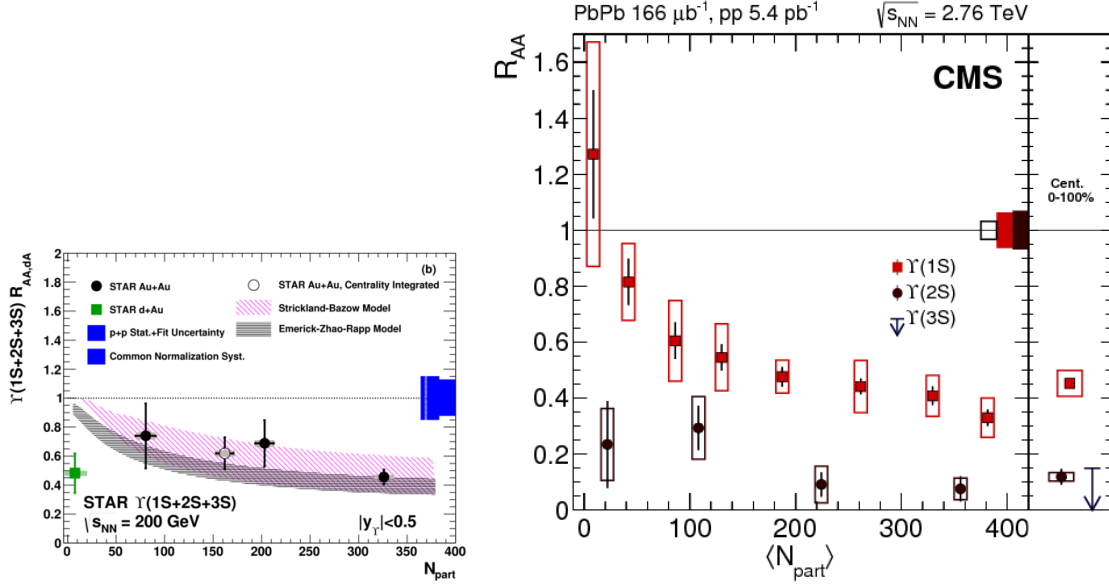


Figure 1-36: The nuclear modifications factor R_{AA} of fully reconstructed Υ as a function of N_{part} measured by the STAR experiment (left) at RHIC and CMS experiment (right) at the LHC are shown above. We can see that R_{AA} of the three Υ states is below 1 for both $N_{part} > 3$. The J/ψ R_{AA} decreases as N_{part} increases, consistent to the increasing creation probability of QGP with larger N_{part} . In addition, a sequential suppression of Υ R_{AA} is observed by the CMS experiment: $R_{AA}^{\Upsilon(1S)} > R_{AA}^{\Upsilon(2S)} > R_{AA}^{\Upsilon(3S)}$, which agrees with the expectation QGP color screening effect.

1.6.3 Macroscopic Properties

Strongly Coupled - color deconfined

Ideal Liquid - Isentropic Expansion - Viscous Hydro

Bjorken

Ulrich

Hydro

Color Opacity

1.6.4 Microscopic Structure

Constituents

Microscopic Kinetics – Transport properties

1.6.5 Open Questions

Today, it has been more than 20 years after the discovery of QGP. However, there are still many open questions.

Relevant Degree of Freedom - Inner workings

1.7 Hard Probes

1.7.1 Jets

1.7.2 Electroweak Probes

1.7.3 Heavy Quarks

1.8 Open Heavy Flavor Physics

1.8.1 Heavy Quark Diffusion

1.8.2 Heavy Quark Energy Loss

1.8.3 Heavy Quark Hadronization

1.8.4 Experimental Observables

Chapter 2

The CMS Detector

2.1 Overview

2.2 Triggers

2.2.1 L1 Hardware Trigger

2.2.2 HLT Trigger

2.3 Tracking System

2.3.1 Silicon Pixel Detector

2.3.2 Silicon Strip Detector

2.3.3 Tracking Algorithm

2.4 Muon System

2.5 Calorimeter System

2.5.1 ECAL

2.5.2 HCAL

2.5.3 Forward HCAL

Chapter 3

Experimental Procedures

3.1 Experimental Setup

3.2 LHC Heavy-Ion Run

3.3 Minimum Biased Trigger

3.4 Dimuon Trigger

3.5 Run Monitoring

3.6 Data Acquisition

Chapter 4

Technical Objects

4.1 Hits

4.2 Clusters

4.3 Tracks

4.4 Vertices

4.5 Muons

Chapter 5

Data Analysis

5.1 Analysis Strategies

5.1.1 Physics Goals

5.1.2 General Workflow

5.1.3 Technical Challenges

5.2 Global Event Observables

5.2.1 Total Number of Events

5.2.2 Centrality Definition

5.2.3 Number of Participants Nucleons

5.2.4 Number of Binary Collisions

5.2.5 Event Multiplicity

5.3 Monte Carlo Simulations

5.3.1 PYTHIA

5.3.2 Hydjet Embedding

78

5.3.3 EvtGen Package

Chapter 6

Conclusions

6.1 Comparison with Other Experiments and Theoretical Models

6.2 Physics Messages Discussion

6.3 Conclusions

6.4 Future Outlooks

Chapter 7

Other Studies

7.1 sPHENIX Heavy Flavor Physics Simulations

7.2 sPHENIX Electromagnetic Calorimeter Studies

7.3 EIC Electromagnetic Calorimeter R&D

Appendix A

Tables

Table A.1: Armadillos

Armadillos	are
our	friends

Appendix B

Figures

Figure B-1: Armadillo slaying lawyer.

Figure B-2: Armadillo eradicating national debt.

List of Symbols

\hbar Reduced Planck constant

c Speed of light in a vacuum inertial frame

p_T Transverse momentum

R_{AA} Nuclear Modification Factor

CERN European Center for Nuclear Research

CMS Compact Muon Solenoid

LHC Large Hadron Collider

Abbreviations

\hbar Reduced Planck constant

c Speed of light in a vacuum inertial frame

p_T Transverse momentum

R_{AA} Nuclear Modification Factor

CERN European Center for Nuclear Research

CMS Compact Muon Solenoid

LHC Large Hadron Collider

References

- [1] M. K. Gaillard, P. D. Grannis, and F. J. Sciulli, “The Standard Model of Particle Physics”, Rev. Mod. Phys. 71 (1999)
- [2] C. D. Roberts, “Nonperturbative effects in QCD at Finite Temperature and Density”, Phys. Part. Nucl. 30 (1999)
- [3] P.A. Zyla et al. (Particle Data Group), “Review of Particle Physics”, Prog. Theor. Exp. Phys. 2020, 083 C01 (2020)
- [4] J. Gross and F. Wilczek, “Ultraviolet behavior of non-abelian gauge theories”, Phys. Rev. Lett. 30, 1343 (1973)
- [5] S. Dürr et al. “Ab Initio Determination of Light Hadron Masses”, Science. 322 (5905): 1224 7 (2008)
- [6] N. Fettes, U.-G. Meißner, and S. Steininger, “Pion-nucleon scattering in chiral perturbation theory I: Isospin-symmetric case”, Nucl. Phys. A 640 (1998)
- [7] J. C. Collins, D. E. Soper, and G. F. Sterman, “Factorization of Hard Processes in QCD”, Adv. Ser. Direct. High Energy Phys. 5 (1989)
- [8] Francesco Becattini, “What is the meaning of the statistical hadronization model?”, J. Phys. Conf. Ser. 5 (2005)
- [9] B. Andersson, G. Gustafson, G. Ingelman, and T. Sjöstrand, “Parton fragmentation and string dynamics”, Phys. Rep. 97 (1983)

- [10] R. J. Fries, V. Greco, and P. Sorensen “Coalescence Models For Hadron Formation From Quark Gluon Plasma”, Ann. Rev. Nucl. Part. Sci. 58 (2008)
- [11] F. Wilczek, “QCD In Extreme Conditions”, Contribution to: 9th CRM Summer School: Theoretical Physics at the End of the 20th Century, 567-636
- [12] E. d'Enterria, David G., et al., “CMS physics technical design report: Addendum on high density QCD with heavy ions”, J. Phys.G 34 (2007)
- [13] E. Altman, “Many-body localization and quantum thermalization”, Nat. Phys. 14, 979 - 983 (2018).
- [14] M. P. Heller, R. A. Janik, and P. Witaszczyk, “Characteristics of Thermalization of Boost-Invariant Plasma from Holography”, Phys. Rev. Lett. 108, 201602 (2012)
- [15] G. Parisi, “Some considerations on the Quark-Gluon Plasma”, Quark Matter 2018 Conference (2018)
- [16]
- [17] H.C. Chandola, G. Punetha, and H. Dehnen, “Dual QCD thermodynamics and quark-gluon plasma”, Nucl. Phys. A 945 (2016)
- [18] R. Stock, “Relativistic Nucleus-Nucleus Collisions and the QCD Matter Phase Diagram”, In *Landolt-Boernstein I 21A: Elementary particles* 7
- [19] T.D. Lee and G.C. Wick, “Vacuum stability and vacuum excitation in a spin-0 field theory”, Phys. Rev. D9 2291(1974)
- [20] J.O. Andersen and T. Brauner, “Linear sigma model at finite density in the 1/N expansion to next-to-leading order”, Phys .Rev. D 78:014030 (2008)
- [21] M. Asakawa and K. Yazaki, “Chiral Restoration at Finite Density and Temperature”, Nucl. Phys. A 504 (1989)
- [22] K. Fukushima, D.E. Kharzeev, and H.J. Warringa, “The Chiral Magnetic Effect”, Phys. Rev. D 78 074033 (2008)

- [23] S. Shi, H. Zhang, D. Hou, and J. Liao, “Signatures of Chiral Magnetic Effect in the Collisions of Isobars”, Phys. Rev. Lett. 125 (2020)
- [24] J. Zhao and F-Q. Wang, “Experimental searches for the chiral magnetic effect in heavy-ion collisions”, Prog. Part. Nucl. Phys. 107 (2019)
- [25] D.E. Kharzeev, J. Liao, S. A. Voloshin, and G. Wang, “Chiral Magnetic and Vortical Effects in High-Energy Nuclear Collisions — A Status Report”, Prog. Part. Nucl. Phys. 88 (2016)
- [26] S. Choudhury, G. Wang, W. He, Y. Hu, and H.Z. Huang, “Background evaluations for the chiral magnetic effect with normalized correlators using a multiphase transport model”, Eur. Phys. J. C 80 (2020)
- [27] H. S. Chung, J. Lee, and D. Kang, “Cornell potential parameters for S-wave heavy quarkonia”, J. Korean Phys. Soc. 52 (2018)
- [28]
- [29] J. Harris and B. Muller, “The Search for the quark-gluon plasma”, Ann. Rev. Nucl. Part. Sci. 46 (1996)
- [30] A. Dumitru, Y. Guo, A. Mócsy, and M. Strickland, “Quarkonium states in an anisotropic QCD plasma”, Phys. Rev. D 79 (2009)
- [31] R. Hagedorn, “Statistical thermodynamics of strong interactions at high energies”, Nuovo Cim. , Suppl. 3 (1965)
- [32] J. Rafelski, “Melting Hadrons, Boiling Quarks”, from Hagedorn Temperature to Ultra-Relativistic Heavy-Ion Collisions at CERN. Springer, Cham.
- [33] C.A. Dominguez, “Color Deconfinement in QCD at Finite Temperature”, Nucl. Phys. B Proc. Suppl.15 (1990)
- [34] K. Rajagopal and F. Wilczek, “The Condensed matter physics of QCD”, part of At the frontier of particle physics. Handbook of QCD. Vol. 1-3 (2000)

- [35] M.B. Gay Ducati, “High Density QCD”, *Braz. J. Phys.* 31 (2001)
- [36] D.E. Kharzeev, “Hot and dense matter: from RHIC to LHC: Theoretical overview”, *Nucl. Phys. A* 827 (2009)
- [37] L.D. McLerran, S. Schlichting, S. Sen, “Space-Time Picture of Baryon Stopping in the Color-Glass Condensate”, *Phys. Rev. D* 99, 074009 (2019)
- [38] F. Gelis, E. Iancu, and J. Jalilian-Marian, R. Venugopalan “The Color Glass Condensate”, *Ann. Rev. Nucl. Part. Sci.* 60 (2010)
- [39] A. Deshpande, Z.-E. Meziani, and J.-W. Qiu, “Towards the next QCD Frontier with the Electron Ion Collider”, *EPJ W of Conf.*, 113, 05019 (2016)
- [40] V.N. Gribov and L.N. Lipatov, *Sov. J. Nucl. Phys.* 15 (1972) 438.
- [41] G. Altarelli and G. Parisi, *Nucl. Phys.* B126 (1977) 298.
- [42] Yu. L. Dokshitzer, *Sov. Phys. JETP* 46 (1977) 641.
- [43] G.P. Salam, “An Introduction to leading and next-to-leading BFKL”, *Acta Phys. Polon. B* 30 (1999)
- [44] K. Rummukainen and H. Weigert, “Universal features of JIMWLK and BK evolution at small x”, *Nucl. Phys. A* 739 (2004)
- [45] C. Marquet, “Open questions in QCD at high parton density”, *Nucl. Phys. A* 904 - 905 (2013)
- [46] L. Zheng, E.C. Aschenauer, J.H. Lee, and B.-W. Xiao, “Probing Gluon Saturation through Dihadron Correlations at an Electron-Ion Collider”, *Phys. Rev. D* 89, 074037 (2014)
- [47] J Jalilian-Marian and X.N. Wang, “Small x gluons in nuclei and hadrons”, *Phys. Rev. D* 60, 054016 (1999)
- [48] V.P. Gonçalves “QCD at high parton density”, *Braz. J. Phys.* 34 (2004)

- [49] F. Arleo and T. Gousset, “Measuring gluon shadowing with prompt photons at RHIC and LHC”, Phys. Lett. B 660 (2008)
- [50] P. Huovinen and P. Petreczky , “QCD Equation of State and Hadron Resonance Gas”, Nucl. Phys. A 837 (2010)
- [51] N. Sarkar and P. Ghosh , “van der Waals hadron resonance gas and QCD phase diagram”, Phys. Rev. C 98, 014907 (2018)
- [52] Jamal. Jalilian-Marian and X.N. Wang, “Shadowing of gluons in perturbative QCD: A comparison of different models”, Phys. Rev. D63, 096001 (2001)
- [53] E. Epelbaum, H.-W. Hammer, and U.G. Meißner, “Modern theory of nuclear forces”, Rev. Mod. Phys. 81 (2009)
- [54] J. Rafelski, "Connecting QGP-Heavy Ion Physics to the Early Universe“, Nucl. Phys. B Proc. Suppl. 243-244 (2013)
- [55] S. M. Sanches Jr., F. S. Navarra, and D. A. Fogaça, “The quark gluon plasma equation of state and the expansion of the early Universe”, Nucl. Phys. A 937 (2015)
- [56] E.S. Fraga and A. Kurkela, “Interacting quark matter equation of state for compact stars”, Astrophys. J. Lett. 781, L25 (2014)
- [57] M. G. Alford, K. Rajagopal, T. Schaefer, A. Schmitt “Color superconductivity in dense quark matter”, Rev. Mod. Phys. 80 (2008)
- [58] M. G. Alford, “Color superconducting quark matter”, Ann. Rev. Nucl. Part. Sci. 51 (2001)
- [59] K. Rajagopal, “Mapping the QCD phase diagram”, Nucl. Phys. A 661 (1999)
- [60] G. Odyniec on behalf of STAR Collaboration, “Beam Energy Scan Program at RHIC (BES I and BES II) – Probing QCD Phase Diagram with Heavy-Ion Collisions”, PoS CORFU2018 (2019)

- [61] Z. Fodor and S.D. Katz, “Critical point of QCD at finite T and mu, lattice results for physical quark masses”, JHEP 04 050 (2004)
- [62] S. Gupta, X. Luo, B. Mohanty, H. G. Ritter, N. Xu, “Scale for the Phase Diagram of Quantum Chromodynamics”, Science 332 (2011)
- [63] R.X. Xu, “Strange quark stars - A Review”, IAU Symp. 214 (2003)
- [64] Y.-Z. Fan, Y.-W. Yu, D. Xu, Z.-P. Jin, X.-F. Wu, D.-M. Wei, and B. Zhang, “A supra-massive magnetar central engine for short GRB 130603B”, Astrophys. J. Lett. 779 (2013)
- [65] Z. G. Dai, S. Q. Wang, J. S. Wang, L. J. Wang, and Y. W. Yu, “The Most Luminous Supernova ASASSN-15lh: Signature of a Newborn Rapidly-Rotating Strange Quark Star”, Astrophys. J. 817 (2016)
- [66]
- [67] D. Trbojevic and S. Peggs, “Required Accuracy of the RHIC Circumference”, United States: N. p., Web. doi:10.2172/1119398 (1993)
- [68] M. J. Rhoades-Brown, “The Heavy Ion Injection Scheme for RHIC”, Proc. of the Workshop on the RHIC Performance (1988)
- [69] D. B. Steski, J. Alessi, J. Benjamin, C. Carlson, M. Manni, P. Thieberger, and M. Wiplich, “Operation of the Relativistic Heavy Ion Collider Au^- ion source”, Review of Scientific Instruments 73, 797 (2002)
- [70] D.B. Steski and P. Thieberger, “Stripping foils at RHIC”, Nucl. Instrum. Meth. A 613 (2010)
- [71] P. Thieberger, L. Ahrens, J. Alessi, J. Benjamin, M. Blaskiewicz, J. M. Brennan, K. Brown, C. Carlson, C. Gardner, W. Fischer, D. Gassner, J. Glenn, W. Mac Kay, G. Marr, T. Roser, K. Smith, L. Snydstrup, D. Steski, D. Trbojevic, N. Tsoupas, V. Zajic, and K. Zeno, “Improved gold ion stripping at 0.1 and

10 GeV/nucleon for the Relativistic Heavy Ion Collider”, Phys. Rev. ST Accel. Beams 11, 011001 (2008)

- [72] L. Evans, “The Large Hadron Collider”, Phil. Trans. R. Soc. A 370 (2012)
- [73] J. Brewer, A. Mazeliauskas, W. van der Schee, “Opportunities of OO and pO collisions at the LHC”, CERN Theory Report: CERN-TH-2021-028 (2021)
- [74] M. Schaumann, R. Alemany-Fernandez, H. Bartosik, T. Bohl, R. Bruce, G-H Hemelsoet, S. Hirlaender, J. Jowett, V. Kain, M. Krasny, J. Molson, G. Papotti, M.S. Camillocci, H. Timko, and J. Wenninger, “First partially stripped ions in the LHC ($^{208}Pb^{81+}$)” J. Phys. Conf. Ser. 1350, 012071 (2019)
- [75] C.Y. Wong, “Introduction to high-energy heavy ion collisions”, Singapore, Singapore: World Scientific (1994) 516 p
- [76] Z.-T. Liang and X.-N. Wang , “Globally Polarized Quark-Gluon Plasma in Non-central A + A Collisions”, Phys.Rev.Lett. 96, 039901 (2006)
- [77] B.Alver and G.Roland, “Collision geometry fluctuations and triangular flow in heavy-ion collisions”, Phys. Rev. C 81, 054905 (2010)
- [78] I. Altsybeev and V. Kovalenko, “Classifiers for centrality determination in proton-nucleus and nucleus-nucleus collisions”, EPJ Web Conf. 137, 11001
- [79] P. Cortese, “Performance of the ALICE Zero Degree Calorimeters and upgrade strategy”, J. Phys. Conf. Ser. 1162, 012006 (2019)
- [80] Oliver Suranyi, “Study of Very Forward Neutrons with the CMS Zero Degree Calorimeter”, Universe 5 10, 210 (2019)
- [81] P. Dmitrieva and I. Pshenichnov, “On the performance of Zero Degree Calorimeters in detecting multinucleon events”, Nucl. Instrum. Meth. A 906 (2018)
- [82] M. L. Miller, K. Reygers, S. J. Sanders and P. Steinberg, ?Glauber modeling in high energy nuclear collisions,? Ann. Rev. Nucl. Part. Sci. 57, 205 (2007)

- [83] R. J. Glauber, "Quantum Optics and Heavy Ion Physics", Nucl. Phys. A 774 (2006)
- [84] J. Chauvin, D. Bebrun, A. Lounis, and M. Buenerd, "Low and intermediate energy nucleus-nucleus elastic scattering and the optical limit of Glauber theory", Phys. Rev. C. 28, 1970 (1983)
- [85] T. Wibig and D. Sobczynska, "Proton-nucleus cross section at high energies", J. Phys. G: Nucl. Part. Phys. 24, 2037 (1998)
- [86] B. B. Back, "Studies of multiplicity in relativistic heavy-ion collisions", J.Phys.Conf.Ser. 5 (2000)
- [87] A. Milov, "Electroweak probes with ATLAS", PoS High-pT2017 016 (2019)
- [88] L. Van Hove, "Theoretical prediction of a new state of matter, the "quark-gluon plasma" (also called "quark matter")", Part of Multiparticle Dynamics. Proceedings, 17th International Symposium, Seewinkel, Austria, June 16-20, 801-818 (1986)
- [89] S. A. Bass, M. Gyulassy, H. Stoecker, and W. Greiner, "Signatures of Quark-Gluon-Plasma formation in high energy heavy-ion collisions: A critical review", J. Phys. G 25 R1-R57 (1999)
- [90] C. Quigg and J. L. Rosner, "Quantum Mechanics with Applications to Quarkonium", Phys. Rept. 56 167-235 (1979)
- [91] P. Petreczky, "Quarkonium in Hot Medium", J. Phys. G 37, 094009 (2010)
- [92] G. S. Bali, H. Neff, T. Duessel, T. Lippert, K. Schilling, "Observation of string breaking in QCD", Phys. Rev. D 71, 114513 (2005)
- [93] P. Petreczky, "Quarkonium in Hot Medium", J. Phys. G 37, 094009 (2010)
- [94] STAR Collaboration, "Measurement of inclusive J/ψ suppression in Au+Au collisions at $\sqrt{s_{NN}} = 200$ GeV through the dimuon channel at STAR", Phys. Lett. B 797, 134917 (2019)

- [95] A. Andronic et. al., “Heavy-flavour and quarkonium production in the LHC era: from proton-proton to heavy-ion collisions”, Eur.Phys.J.C 76, 107 (2016)
- [96] STAR Collaboration, “Suppression of Υ production in d+Au and Au+Au collisions at $\sqrt{s_{NN}} = 200$ GeV”, Phys. Lett. B 735, 127-137 (2014)
- [97] CMS Collaboration, “Suppression of $\Upsilon(1S)$, $\Upsilon(2S)$, and $\Upsilon(3S)$ production in PbPb collisions at $\sqrt{s_{NN}} = 200$ GeV”, Phys. Lett. B 770 357-379 (2017)
- [98] ZEUS Collaboration, “Forward jet production in deep inelastic ep scattering and low-x parton dynamics at HERA”, Phys. Lett. B 632 13-26 (2006)
- [99] STAR Collaboration, “Disappearance of back-to-back high p_T hadron correlations in central Au+Au collisions at $\sqrt{s_{NN}} = 200$ GeV”, Phys.Rev.Lett. 90, 082302 (2003)
- [100] ALICE Collaboration, “Measurements of inclusive jet spectra in pp and central Pb-Pb collisions at $\sqrt{s_{NN}} = 5.02$ TeV”, Phys. Rev. C 101, 034911 (2020)
- [101] P. Bozek and I. Wyskiel, “Directed flow in ultrarelativistic heavy-ion collisions”, Phys. Rev. C 81, 054902 (2010)
- [102] CMS Collaboration, “Constraints on the chiral magnetic effect using charge-dependent azimuthal correlations in pPb and PbPb collisions at the CERN Large Hadron Collider”, Phys. Rev. C 97, 044912 (2018)
- [103] A. M. Poskanzer and S.A. Voloshin, “Methods for analyzing anisotropic flow in relativistic nuclear collisions”, Phys.Rev.C 58 1671-1678 (1998)
- [104] R. S. Bhalerao, J.-Y. Ollitrault, “Eccentricity fluctuations and elliptic flow at RHIC”, Phys. Lett. B 641, 260-264 (2006)
- [105] STAR Collaboration, “Elliptic flow in Au+Au collisions at $\sqrt{s_{NN}} = 130$ GeV”, Phys. Rev. Lett. 86, 402-407 (2001)
- [106] ALICE Collaboration, “Elliptic flow of charged particles in Pb-Pb collisions at 2.76 TeV”, Phys. Rev. Lett. 105, 252302 (2010)

- [107]
- [108] J. Rafelski and B. Muller, “Strangeness Production in the Quark-Gluon Plasma”, Phys. Rev. Lett. 48, 1066 (1982)
- [109] STAR Collaboration, “Measurements of ϕ meson production in relativistic heavy-ion collisions at RHIC”, Phys. Rev. C 79, 064903 (2009)
- [110] ALICE Collaboration, “Enhanced production of multi-strange hadrons in high-multiplicity proton-proton collisions”, Nature Phys. 13, 535-539 (2017)
- [111] U. W. Heinz and M. Jacob, “Evidence for a new state of matter: An Assessment of the results from the CERN lead beam program”, CERN Special Seminar Report, (2000)